Pathogenic mutations in the chromokinesin KIF22 disrupt anaphase chromosome segregation

Alex F. Thompson[1], Patrick R. Blackburn[2,3], Dusica Babovic-Vuksanovic[2,4], Jane B. Lian[5], Eric W. Klee[6], Jason K. Stumpff[1*]

[1]Molecular Physiology and Biophysics, University of Vermont, Burlington, VT
[2]Laboratory Medicine and Pathology, Mayo Clinic, Rochester, MN
[3]Pathology, St. Jude Children's Research Hospital, Memphis, TN
[4]Clinical Genomics, Mayo Clinic, Rochester, MN
[5]Biochemistry, University of Vermont, Burlington, VT
[6]Biomedical Informatics, Mayo Clinic, Rochester, MN
*Corresponding author, jason.stumpff@uvm.edu

ABSTRACT

The chromokinesin KIF22 uses plus end-directed motility and direct binding to chromosome arms to generate pushing forces that contribute to mitotic chromosome congression and alignment. Mutations in the motor domain of KIF22 have been identified in patients with abnormal skeletal development, and we report the identification of a patient with a novel mutation in the coiled-coil domain of the KIF22 tail. The mechanism by which these mutations affect development is unknown. We assessed whether pathogenic mutations affect the function of KIF22 in mitosis and demonstrate that mutations do not result in a loss of KIF22 function. Pathogenic mutations did not alter the localization or prometaphase function of KIF22. Instead, mutations disrupted chromosome segregation in anaphase, resulting in reduced proliferation, abnormal daughter cell nuclear morphology and, in a subset of cells, cytokinesis failure. This phenotype could be explained by a failure of KIF22 to inactivate in anaphase. Consistent with this model, a phosphomimetic mutation, which constitutively activates the motor, phenocopied the effects of pathogenic mutations. These findings offer insight into the mechanism by which mutations in KIF22 may affect human development, the balance between polar ejection forces and antiparallel microtubule sliding in anaphase, and potential mechanisms of KIF22 regulation.

INTRODUCTION

Mitosis requires mechanisms that mechanically control chromosome movements to ensure equal segregation of chromosomes to daughter cells. Forces that move mitotic chromosomes are generated by microtubule dynamics within the mitotic spindle and by molecular motor proteins. The chromokinesin KIF22 (or Kid, kinesin-like DNA-binding protein) is a plus-end directed member of the kinesin-10 family (Yajima et al., 2003). KIF22 and its orthologs, including

39 Nod (*Drosophila melanogaster*) (Zhang, Knowles, Goldstein, & Hawley, 1990) and Xkid (*Xenopus*
40 *laevis*) (Antonio et al., 2000; Funabiki & Murray, 2000; Takagi, Itabashi, Suzuki, & Ishiwata, 2013),
41 generate forces that move chromosomes away from the spindle poles. Structurally, KIF22
42 contains a conserved kinesin motor domain responsible for ATP hydrolysis and microtubule
43 binding (Tokai et al., 1996; Yajima et al., 2003), a second microtubule binding domain in the tail
44 (Shiroguchi, Ohsugi, Edamatsu, Yamamoto, & Toyoshima, 2003), a predicted coiled-coil domain
45 (Shiroguchi et al., 2003), and a C-terminal DNA binding domain which includes a helix-hairpin-
46 helix motif (Tokai et al., 1996) **(Figure 1A)**.

47 In interphase, KIF22 localizes to the nucleus (Levesque & Compton, 2001; Tokai et al.,
48 1996). As cells enter mitosis, chromosomes condense and KIF22 binds along chromosome arms
49 (Levesque & Compton, 2001; Tokai et al., 1996). In prometaphase, chromosomes must congress
50 and align at the center of the spindle. The interactions of the KIF22 motor domain with spindle
51 microtubules and the KIF22 tail domain with chromosome arms allows the motor to generate polar
52 ejection forces (Bieling, Kronja, & Surrey, 2010; Brouhard & Hunt, 2005), which push the arms of
53 chromosomes away from the spindle poles and towards the center of the spindle (Marshall,
54 Marko, Agard, & Sedat, 2001; Rieder & Salmon, 1994; Rieder, Davison, Jensen, Cassimeris, &
55 Salmon, 1986), contributing to chromosome congression in prometaphase (Iemura & Tanaka,
56 2015; Levesque & Compton, 2001; Wandke et al., 2012), as well as chromosome arm orientation
57 (Levesque & Compton, 2001; Wandke et al., 2012). In metaphase, polar ejection forces also
58 contribute to chromosome oscillation and alignment (Antonio et al., 2000; Funabiki & Murray,
59 2000; Levesque & Compton, 2001; Levesque, Howard, Gordon, & Compton, 2003; Stumpff,
60 Wagenbach, Franck, Asbury, & Wordeman, 2012; Takagi et al., 2013; Tokai-Nishizumi, Ohsugi,
61 Suzuki, & Yamamoto, 2005). Purified KIF22 is monomeric (Shiroguchi et al., 2003), and the forces
62 generated by KIF22 on chromosomes arms may represent the collective action of many
63 monomers. In anaphase, KIF22 is inactivated to reduce polar ejection forces and allow
64 chromosomes to segregate towards the spindle poles (Soeda, Yamada-Nomoto, & Ohsugi, 2016;
65 Su et al., 2016).

66 The generation of polar ejection forces by KIF22 is regulated by the activity of cyclin-
67 dependent kinase 1 (CDK1)/cyclin B, which is high in prometa- and metaphase, and drops sharply
68 at the metaphase to anaphase transition when cyclin B is degraded (Hershko, 1999; Morgan,
69 1995). KIF22 is phosphorylated by CDK1/cyclin B at T463, a residue in the tail of the motor
70 between the second microtubule binding and coiled-coil domains. Phosphorylation of T463 is
71 required for polar ejection force generation in prometa- and metaphase, and dephosphorylation
72 of T463 is necessary for the suspension of polar ejection forces to allow chromosome segregation

in anaphase (Soeda et al., 2016). Reduced polar ejection forces in anaphase are one component of an overall shift in force balance at the metaphase to anaphase transition as microtubule dynamics and motor activities change to promote anaphase chromosome segregation rather than metaphase congression. In addition to its activity, the expression level of KIF22 is also regulated as the cell cycle progresses. Expression is highest in G2 phase and mitosis, and drops as cells exit mitosis (Germani et al., 2000; Yount, Zong, & Walczak, 2015).

Mutations in KIF22 have been identified in patients with a developmental disorder, spondyloepimetaphyseal dysplasia with joint laxity, leptodactylic type (SEMDJL2, also referred to as Hall Type or lepto-SEMDJL) (Boyden et al., 2011; Min et al., 2011; Tüysüz, Yılmaz, Erener-Ercan, Bilguvar, & Günel, 2014). Four point mutations in two amino acids have been reported in SEMDJL2 patients (Boyden et al., 2011; Min et al., 2011; Tüysüz et al., 2014) **(Figure 1A)**. These mutations occur in adjacent residues P148 and R149 in the α2 helix of the KIF22 motor domain **(Figure 1B)**. P148 and R149 are conserved in kinesin-10 family members across species **(Figure 1C)** and in many human members of the kinesin superfamily **(Figure 1D)**. All identified patients are heterozygous for a single mutation in KIF22. Mutations dominantly cause SEMDJL2, and patients with both *de novo* and inherited mutations in KIF22 have been identified (Boyden et al., 2011; Min et al., 2011).

Although KIF22 mRNA is expressed throughout the body (Human Protein Atlas, http://www.proteinatlas.org (Uhlen et al., 2015)), the effects of these mutations are largely tissue-specific, and the development of the skeletal system is most affected in SEMDJL2 patients. A primary symptom of SEMDJL2 is short stature, resulting from shortening of both the trunk and the limbs. Additionally, patients present with joint laxity, midface hypoplasia, scoliosis, and leptodactyly, a narrowing of the fingers (Boyden et al., 2011; Min et al., 2011). In very young children, the softness of the cartilage in the larynx and trachea can cause respiratory issues (Boyden et al., 2011). Growth plate radiology demonstrated delayed maturation of the metaphyses and epiphyses in SEMDJL2 patients, and symptoms became more pronounced as patients aged (Tüysüz et al., 2014). Leptodactyly, specifically, was only observed in older (young adult) patients (Boyden et al., 2011).

Pathogenic mutations in the KIF22 motor domain were predicted to be loss of function mutations (Min et al., 2011). However, KIF22 knockout in mice did not affect skeletal development. Loss of KIF22 was lethal early in embryogenesis for approximately 50% of embryos, but mice that survived past this point developed to adulthood and demonstrated no gross abnormalities or pathologies (Ohsugi et al., 2003). As such, the cellular mechanism by which mutations in KIF22 affect development is unknown.

107 Here we characterize an additional patient with a mutation in KIF22 and assess the effect
108 of previously reported and novel pathogenic mutations on the function of KIF22 in mitosis. We
109 demonstrate that mutations are not loss of function mutations, and do not alter the localization of
110 the motor or the generation of polar ejection forces in prometaphase. Instead, mutations disrupt
111 anaphase chromosome segregation, consistent with continued KIF22 activation and consequent
112 polar ejection force generation in anaphase. Defects in anaphase chromosome segregation affect
113 daughter cell nuclear morphology and, in a subset of cells, prevent cytokinesis. These findings
114 demonstrate that anaphase inactivation of KIF22 is critical for daughter cell fitness. As such,
115 mitotic defects may contribute to pathogenesis in patients with KIF22 mutations. Additionally, we
116 demonstrate that aberrant polar ejection force generation in anaphase is sufficient to affect the
117 movements of not only the chromosomes but also the spindle poles, offering insight into the
118 balance of forces required in anaphase for accurate chromosome segregation.
119
120 **RESULTS**
121 **A novel mutation in KIF22 affects development**
122 We report the identification and characterization of a patient with a novel mutation in KIF22
123 **(Figure 1E)**. The patient is a 15-year-old male with a history of short stature, cryptorchidism and
124 shawl scrotum, minimal scoliosis, secondary enuresis, and skin hyperpigmentation. He presented
125 for evaluation at 9 years of age. At that time, his height was just below 3% for age, weight was at
126 40% for age, and BMI was 82% for age. He was noted to have relative macrocephaly, with a head
127 circumference at 93% for age. He had a broad forehead and hypertelorism, round face, flaring of
128 eyebrows, and ankyloglossia. He also had mild brachydactyly **(Figure 1F)**. He had a history of
129 short stature since infancy, but followed a trajectory close to the third percentile. Growth hormone
130 and thyroid function were normal. Bone age showed a normal, age-appropriate bone maturation
131 with normal epiphyseal ossification centers. However, skeletal survey at age 11 years disclosed
132 mild scoliosis of 14 degrees, as well as mild increase of the central anteroposterior diameter of
133 several lower thoracic vertebrae with mild "bullet-shaped" appearance, mild posterior scalloping
134 of the lumbar vertebrae, and mild foreshortening of both 4th metacarpals **(Figure 1G)**.
135 Genetic testing was performed to determine the cause of these developmental
136 differences. Clinical whole exome sequencing revealed two variants of uncertain significance: a
137 maternally inherited heterozygous *SLC26A2* variant [NM_000112.3(SLC26A2): c.1046T>A
138 (p.F349Y)] (SCV000782516.1) as well as a *de novo* heterozygous *KIF22* variant
139 [NM_007317.3(KIF22):c.1424T>G (p.V475G)] (SCV000782515.1) **(Figure 1E)**. The *SLC26A2*
140 gene encodes the diastrophic dysplasia sulfate transporter (Haila et al., 2001; Rossi & Superti-

141 Furga, 2001). However, results of carbohydrate deficient transferrin testing were not consistent
142 with a congenital disorder of glycosylation (transferrin tri-sialo/di-oligo ratio 0.07).
143 The c.1424T>G, p.(V475G) *KIF22* variant has not been observed previously in the
144 Genome Aggregation Database (gnomAD). This missense variant is predicted to be deleterious
145 by Sorting Intolerant from Tolerant (SIFT) (Vaser, Adusumalli, Leng, Sikic, & Ng, 2015), benign
146 by Polymorphism Phenotyping (PolyPhen-2) (Adzhubei et al., 2010), and disease causing by
147 MutationTaster (Schwarz, Rödelsperger, Schuelke, & Seelow, 2010). According to American
148 College of Medical Genetics 2015 criteria, the variant was classified as a variant of uncertain
149 significance (VUS). V475 is located in the coiled-coil domain in the tail of KIF22 **(Figure 1A)**. This
150 residue is conserved in most kinesin-10 family members across species **(Figure 1C)**. However,
151 the tail domains of kinesin motors diverge in both structure and function, and as such meaningful
152 alignments to assess the conservation of V475 across the human kinesin superfamily were not
153 possible.

Figure 1

A

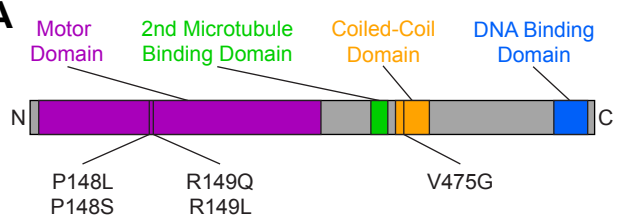

B

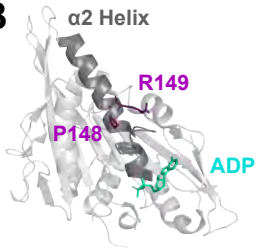

C

Homo sapiens	141	PEQPGVIPRALMDLLQLTREE	161	468	RMVLMKTVEEKDLEI	482
Mus musculus	136	PEQPGVIPRALMDLLQLAREE	156	463	RMVLMKTVEEKNLEI	477
Xenopus laevis	130	PNQPGVIPRAVRDLLQMSRTA	150	450	RMALLKKWEESQMEI	464
Danio rerio	117	QEQPGVIPRAVKEVFNLVGAQ	137	426	RLNLLKTVAQSRKEI	440
Bos taurus	136	PEQPGVIPRALMDLLQLTREE	156	463	RMVLMKTVEEKDLEI	477
Drosophila melanogaster	107	PEHLGILPRALGDIFERVTAR	127	445	NSTLMGIVEETEPK-	459

D

KIF22	141	PEQPGVIPRALMDLLQLTREE	161
KIF5A	122	PQLMGIIPRIARDIFNHIYSM	142
KIF5B	121	PEGMGIIPRIVQDIFNYIYSM	141
KIF5C	122	PQLMGIIPRIAHDIFDHIYSM	142
KIF3A	116	PELRGIIPNSFAHIFGHIAKA	136
KIF3B	112	PEKRGVIPNSFDHIFTHISRS	132
KIF3C	113	PELRGVIPNAFEHIFTHISRS	133
KIF17	107	PSQRGIIPRAFEHVFESVQCA	127
KIF1A	112	KDQQGIIPQLCEDLFSRINDT	132
KIF1B	112	ESQAGIIPQLCEELFEKINDN	132
KIF1C	112	PGQQGIVPQLCEDLFSRVSEN	132
KIF13A	116	-EQLGLIPRLCCALFKRISLE	135
KIF13B	117	-DQPGLIPRLCSGLFERTQKE	136
KIF4B	108	EPTVGIIPRVIQLLFKEIDKK	128
KIF7	114	EDEQGIVPRAMAEAFKLIDEN	135
KIF21A	108	EEELGIISRAVKHLFKSIEEK	128
KIF21B	107	EEEQGIIPRAIAHLFGGIAER	127
KIF11	128	DPLAGIIPRTLHQIFEKLTD-	147
KIF20A	176	--DGGILPRSLALIFNSLQGQ	194
KIF20B	168	--NIGILPRTLNVLFDSLQER	196
KIF23	128	--EGGLLPRCLDMIFNSIGSF	146
KIF10	101	--HLGVIPRAIHDIFQKIKKF	119
KIF18A	125	ADEPGVMYLTMLHLYKCMDEI	145
KIF18B	121	EGDPGIMYLTTVELYRRLEAR	141
KIF19	116	DQEPGIYVQTLNDLFRAIEET	136
KIF6	113	YSDRGIIPRTLSYIFEQLQKD	133
KIF9	109	YKHRGILPRALQQVFRMIEER	129
KIF12	128	PSLAGIMQRTFAWL---LDRV	145
KIF15	130	HNLRGVIPRSFEYLFSLIDRE	130

E

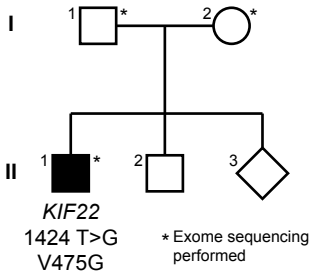

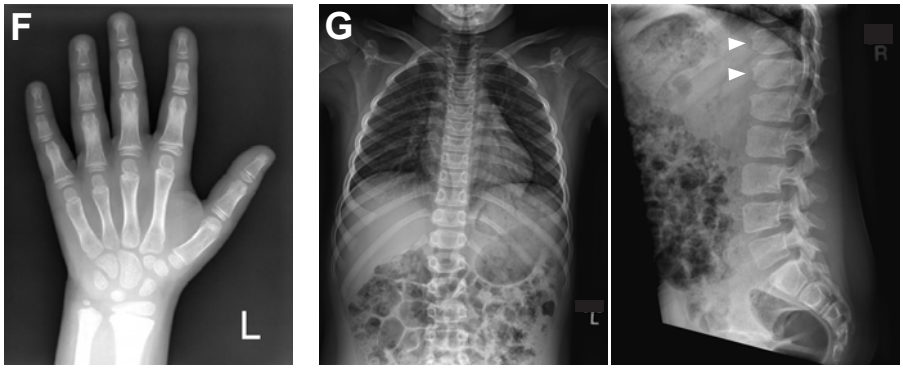

154 **Figure 1. Identification of a novel pathogenic mutation in the tail of KIF22.**
155 **(A)** Schematic of the domains of KIF22 with pathogenic mutations in the motor domain (magenta)
156 and coiled-coil domain (yellow) indicated. **(B)** Location of amino acids P148 and R149 in the
157 alpha-2 helix of the KIF22 motor domain (PDB 6NJE). **(C)** Alignment of amino acid sequences of
158 kinesin-10 family members to assess conservation of motor domain (P148 and R149, left) and
159 coiled-coil domain (V475G, right) residues across species. **(D)** Alignment of amino acid
160 sequences of human kinesin motors to assess conservation of motor domain residues across the
161 kinesin superfamily. For C and D, alignments were performed using Clustal Omega. **(E)** Pedigree
162 identifying the *de novo* V475G (1424 T>G) mutation. **(F)** Radiograph of the patient's hand,
163 posteroanterior view. **(G)** Radiographs of the patient's spine. Left: anteroposterior view of the
164 chest, right: lateral view of the lumbo-sacral spine. Arrowheads indicate "bullet-shaped" vertebrae.

165 **Pathogenic mutations in KIF22 do not disrupt the localization of the motor**

166 To assess the effect of published pathogenic mutations in the motor domain and the novel
167 pathogenic mutation in the tail on the function of KIF22 in mitosis, we generated human cervical
168 adenocarcinoma (HeLa-Kyoto) cell lines with inducible expression of KIF22-GFP. Treatment of
169 these cells with doxycycline induced KIF22-GFP expression at a level approximately two- to three-
170 fold higher than the level of expression of endogenous KIF22 as measured by
171 immunofluorescence **(Figure S1A-C)**. To facilitate both overexpression of and rescue with KIF22-
172 GFP constructs, siRNA-resistant silent mutations were introduced into exogenous KIF22 **(Figure**
173 **S1D-E)**. Initial experiments were performed using HeLa-Kyoto cell lines expressing each known
174 pathogenic mutation in KIF22 (P148L, P148S, R149L, R149Q, and V475G), and a subset of
175 experiments then focused on cells expressing one representative motor domain mutation
176 (R149Q) or the coiled-coil domain mutation in the tail (V475G). Additionally, we generated
177 inducible retinal pigmented epithelial (RPE-1) cell lines expressing wild type and mutant KIF22-
178 GFP to assess any differences between the consequences of expressing mutant KIF22 in
179 aneuploid cancer-derived cells (HeLa-Kyoto) and genomically stable somatic cells. RPE-1 cells
180 are human telomerase reverse transcriptase (hTERT)-immortalized (Bodnar et al., 1998), and
181 metaphase chromosome spreads demonstrated that these cell lines are near-diploid, with a
182 modal chromosome number of 46, even after selection to generate stable cell lines **(Figure S1F-**
183 **G)**. The expression level of siRNA-resistant KIF22-GFP in RPE-1 cell lines was approximately
184 four- to seven-fold higher than the level of expression of endogenous KIF22 **(Figure S1H-K)**.

185 KIF22 localizes to the nucleus in interphase, and primarily localizes to chromosomes and
186 spindle microtubules during mitosis (Tokai et al., 1996). KIF22-GFP with pathogenic mutations
187 demonstrated the same localization pattern throughout the cell cycle as wild type motor (**Figure**
188 **2A)**. In all cell lines, KIF22-GFP was localized to the nucleus in interphase cells and was bound
189 to condensing chromosomes in prophase. In prometaphase, metaphase, and anaphase mutant
190 and wild type KIF22-GFP localized primarily to chromosome arms, with a smaller amount of motor
191 signal visible on the spindle microtubules. The same localization patterns were seen for mutant
192 and wild type KIF22-GFP expressed in RPE-1 cells **(Figure S2A)**.

193 Since mutations did not grossly disrupt localization of KIF22-GFP, fluorescence recovery
194 after photobleaching (FRAP) was used to compare the dynamics of mutant and wild type KIF22
195 localization. In interphase nuclei, KIF22-GFP signal recovered completely 220 seconds after
196 bleaching (97% ± 3% of intensity before bleaching, mean ± SEM), indicating a dynamic pool of
197 KIF22-GFP **(Figure 2B and S2B)**. Similar high recovery percentages were also measured in
198 interphase nuclei of cells expressing KIF22-GFP R149Q and KIF22-GFP V475G (100% ± 6% and

199 103% ± 7% at 220 seconds, respectively) **(Figure 2E and 2H)**. In contrast, KIF22-GFP recovery
200 was minimal in cells bleached during metaphase (25% ± 3% of intensity before bleaching) **(Figure**
201 **2C and S2B)** and anaphase (35% ± 6%) **(Figure 2D and S2B)** during the same time period,
202 suggesting that KIF22 stably associates with mitotic chromosomes. Pathogenic mutations did not
203 change these localization dynamics; recovery percentages in mitosis were also low in cells
204 expressing KIF22-GFP R149Q (32 ± 3% in metaphase, 39 ± 6% in anaphase) **(Figure 2F and**
205 **2G)** and KIF22-GFP V475G (29 ± 2% in metaphase, 35 ± 6% in anaphase) **(Figure 2I and 2J)**.
206 These data indicate that pathogenic mutations do not alter the localization of KIF22 to
207 chromosomes and spindle microtubules, and do not alter KIF22 localization dynamics.

Supplemental Figure 1

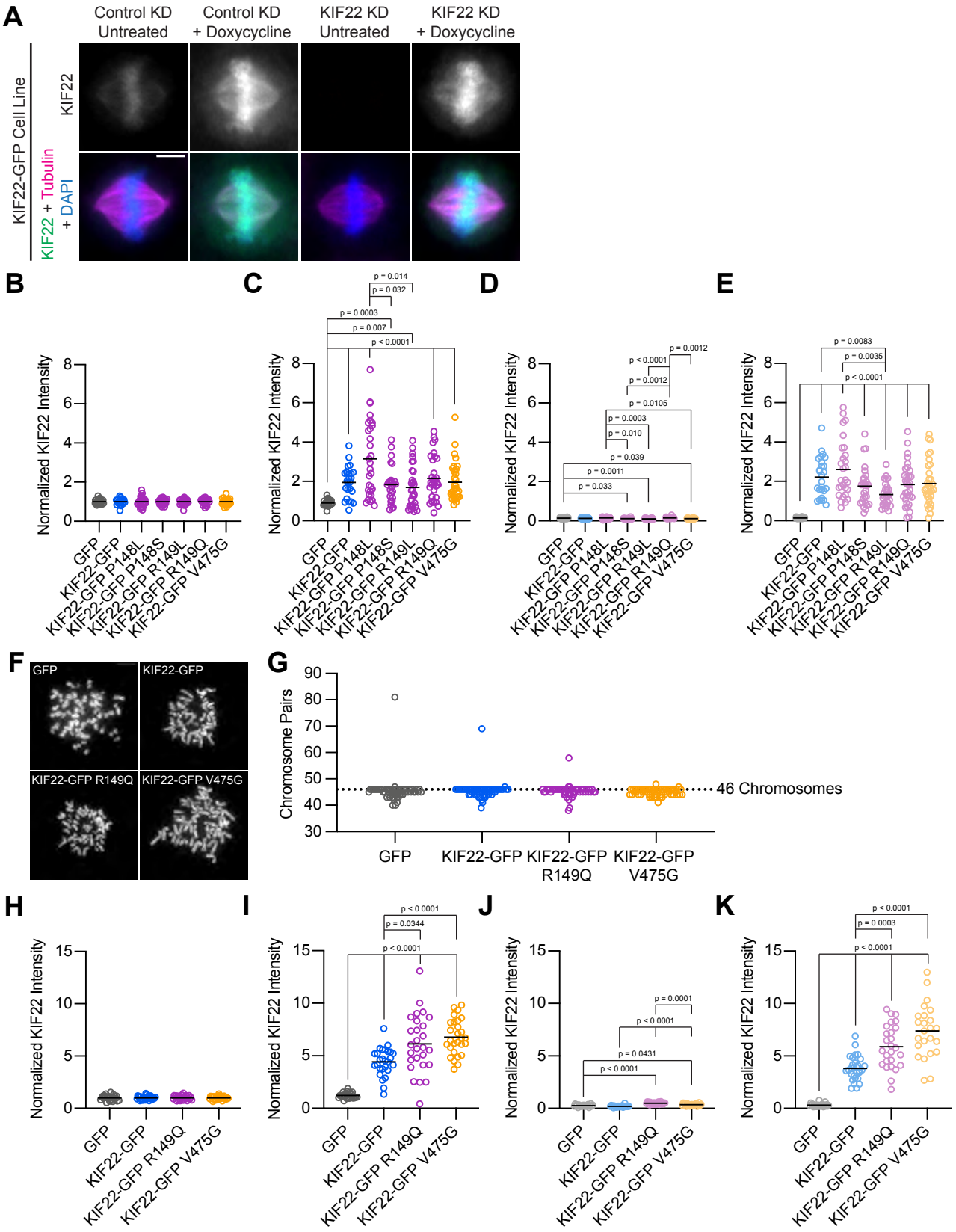

208 **Supplemental Figure 1. HeLa-Kyoto and RPE-1 stable cell lines express mutant KIF22.**
209 **(A**) Immunofluorescence images of HeLa-Kyoto cells expressing KIF22-GFP under the control of
210 a doxycycline inducible promoter. Images are maximum intensity projections in z of five frames
211 at the center of the spindle. Fixed approximately 24 hours after siRNA transfection and treatment
212 with doxycycline to induce expression. Scale bar 5 μm. KD: knockdown. **(B-E)** Quantification of
213 KIF22 fluorescence intensity in untreated HeLa-Kyoto cells transfected with control siRNA (B),
214 cells treated with doxycycline to induce expression and transfected with control siRNA (C),
215 untreated cells transfected with KIF22 siRNA (D), and cells treated with doxycycline and
216 transfected with KIF22 siRNA (E) normalized to the mean intensity of uninduced, control
217 knockdown cells (endogenous KIF22 expression level) for each cell line (B). 21-33 HeLa-Kyoto
218 cells per condition from 3 experiments. **(F)** DAPI-stained metaphase chromosome spreads from
219 uninduced RPE-1 cell lines with inducible expression of GFP, KIF22-GFP, KIF22-GFP R149Q, or
220 KIF22-GFP V475G. Scale bar 10 μm. Images are representative of 3 experiments. **(G)** Numbers
221 of chromosome pairs counted in metaphase spreads prepared from RPE-1 stable cell lines.
222 Dashed line indicates the expected chromosome number for diploid human cells (46). The mode
223 for each cell line is 46. 53-58 spreads per condition from 3 experiments. **(H-K)** Quantification of
224 KIF22 fluorescence intensity in untreated RPE-1 cells transfected with control siRNA (H), cells
225 treated with doxycycline to induce expression and transfected with control siRNA (I), untreated
226 cells transfected with KIF22 siRNA (J), and cells treated with doxycycline and transfected with
227 KIF22 siRNA (K) normalized to the mean intensity of uninduced, control knockdown cells for each
228 cell line (H). 21-29 RPE-1 cells per condition from 3 experiments. For B-E and H-K, bars indicate
229 means. p values from Brown-Forsythe and Welch ANOVA with Dunnett's T3 multiple comparisons
230 test. p values are greater than 0.05 for comparisons without a marked p value.

Figure 2

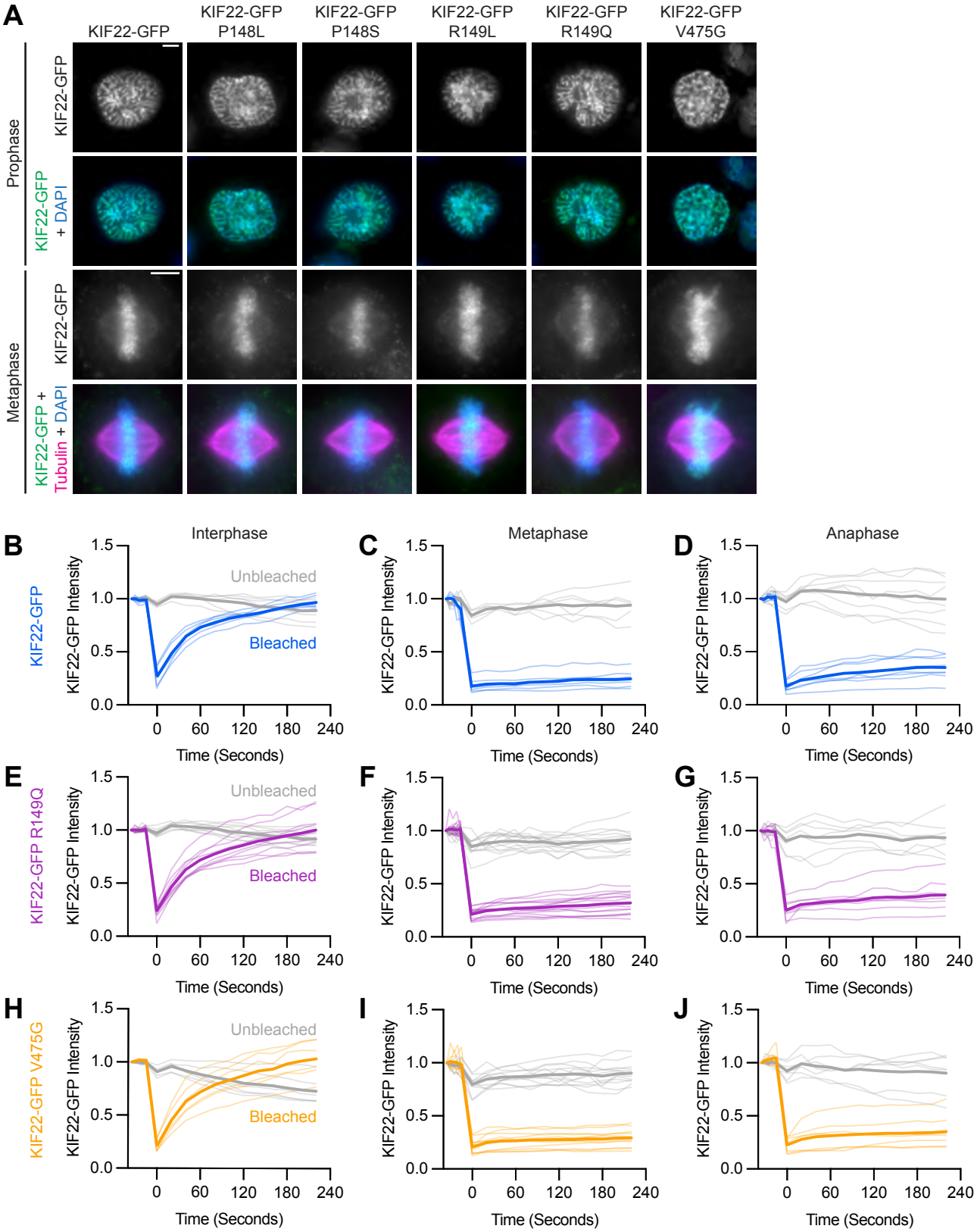
A
KIF22-GFP
KIF22-GFP P148L
KIF22-GFP P148S
KIF22-GFP R149L
KIF22-GFP R149Q
KIF22-GFP V475G
Prophase
Metaphase
KIF22-GFP
KIF22-GFP + DAPI
KIF22-GFP + Tubulin + DAPI
B
C
D
E
F
G
H
I
J
Interphase
Metaphase
Anaphase
KIF22-GFP
KIF22-GFP R149Q
KIF22-GFP V475G
KIF22-GFP Intensity
Time (Seconds)
Unbleached
Bleached
0.0
0.5
1.0
1.5
0
60
120
180
240

231 **Figure 2. Pathogenic mutations in KIF22 do not disrupt the localization of the motor.**
232 **(A)** Immunofluorescence images of HeLa-Kyoto cells expressing KIF22-GFP constructs in
233 prophase (top two rows) and metaphase (bottom two rows). KIF22-GFP was visualized using an
234 anti-GFP antibody. Images are maximum intensity projections in z of five frames at the center of
235 the spindle (metaphase cells) or maximum intensity projections in z of two frames (prophase
236 cells). Fixed approximately 24 hours after treatment with doxycycline to induce expression. Scale
237 bars 5 μm. **(B-J)** Fluorescence recovery after photobleaching (FRAP) of KIF22-GFP (B-D), KIF22-
238 GFP R149Q (E-G), and KIF22-GFP V475G (H-J) in interphase nuclei (B, E, H) or on metaphase
239 (C, F, I) or anaphase (D, G, J) chromosomes. Bleaching occurred at time zero. Thin lines are
240 traces from individual cells and thick lines represent means. Intensity values are normalized to
241 the KIF22-GFP intensity in the first imaged frame before bleaching. 6-14 cells from 3-5
242 experiments per condition.

Supplemental Figure 2

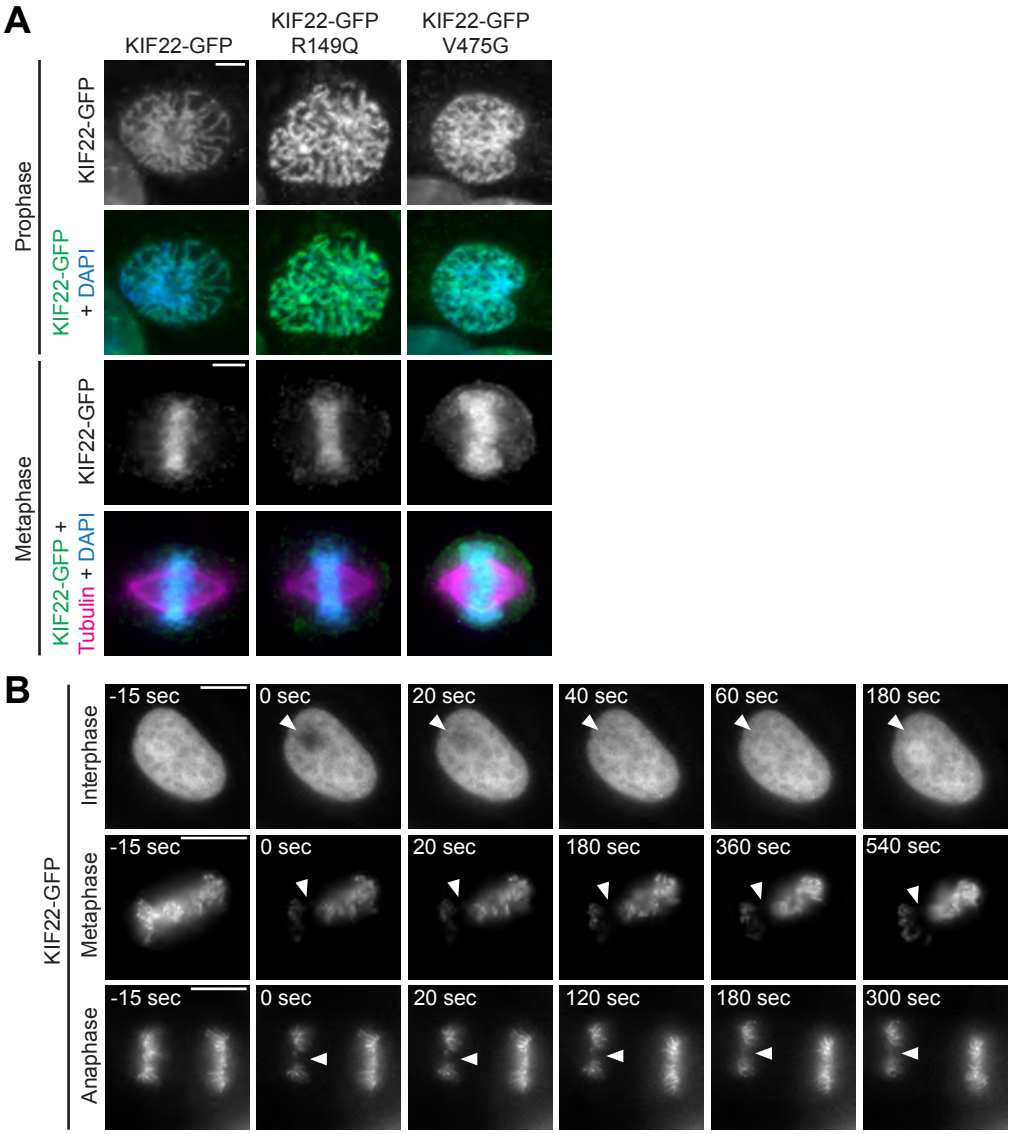

243 **Supplemental Figure 2. Pathogenic mutations in KIF22 do not disrupt the localization of**
244 **the motor in RPE-1 cells.**
245 **(A)** Immunofluorescence images of RPE-1 cells expressing KIF22-GFP constructs in prophase
246 (top two rows) and metaphase (bottom two rows). KIF22-GFP was visualized using an anti-GFP
247 antibody. Images are maximum intensity projections in z of five frames at the center of the spindle
248 (metaphase cells) or maximum intensity projections in z of three frames (prophase cells). Fixed
249 approximately 18 hours after treatment with doxycycline to induce expression. Scale bars 5 μm.
250 **(B)** Time-lapse images of fluorescence recovery after photobleaching (FRAP) in HeLa-Kyoto cells
251 expressing KIF22-GFP. Bleaching occurred at time zero, and arrowheads indicate bleached area.
252 Scale bars 10 μm. Images are representative of 3 or more experiments.

253 **Mutations do not reduce polar ejection forces**

254 In prometaphase and metaphase, KIF22 contributes to chromosome congression and
255 alignment by generating polar ejection forces (Brouhard & Hunt, 2005; Levesque & Compton,
256 2001; Stumpff et al., 2012; Wandke et al., 2012). In cells treated with monastrol to inhibit
257 Eg5/KIF11 and generate monopolar spindles, polar ejection forces push chromosomes away from
258 a single central spindle pole (Levesque & Compton, 2001) **(Figure 3A)**. A loss of KIF22 function
259 causes chromosomes to collapse in towards the pole in this system (Levesque & Compton, 2001)
260 **(Figure 3A)**. To determine whether overexpression of KIF22-GFP with pathogenic mutations has
261 a dominant effect on polar ejection force generation, wild type or mutant KIF22-GFP-expressing
262 HeLa-Kyoto cells were treated with monastrol to induce mitotic arrest with monopolar spindles.
263 Relative polar ejection forces were compared by measuring the distance from the spindle pole to
264 the maximum DAPI signal **(Figure 3A)**. Expression of mutant motor did not reduce polar ejection
265 forces **(Figure 3B and 3C)**. Rather, expression of KIF22-GFP R149L and R149Q significantly
266 increased the distance from the pole to the maximum DAPI signal (R149L 4.6 $\pm$ 0.13 μm, R149Q
267 4.3 $\pm$ 0.11 μm, GFP control 3.7 $\pm$ 0.04 μm, mean $\pm$ SEM), indicating higher levels of polar ejection
268 forces in these cells.

269 The same assay was used to test whether mutant KIF22 could rescue polar ejection force
270 generation in cells depleted of endogenous KIF22. In control cells expressing GFP, depletion of
271 endogenous KIF22 resulted in the collapse of chromosomes towards the pole **(Figure 3B)**, and
272 the distance from the pole to the maximum DAPI signal was reduced to 1.6 $\pm$ 0.11 μm, indicating
273 a loss of polar ejection forces **(Figure 3D)**. This reduction was not observed in cells expressing
274 wild type or mutant KIF22-GFP, demonstrating that KIF22-GFP with pathogenic mutations is
275 capable of generating polar ejection forces **(Figure 3B and 3D)**.

276 Together, the localization of mutant KIF22 and the ability of mutant KIF22 to generate
277 polar ejection forces indicate that pathogenic mutations P148L, P148S, R149L, R149Q, and
278 V475G do not result in a loss of KIF22 function during early mitosis.

Figure 3

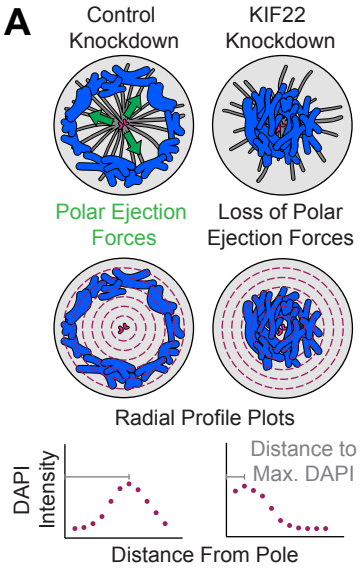
A
Control Knockdown
KIF22 Knockdown
Polar Ejection Forces
Loss of Polar Ejection Forces
Radial Profile Plots
DAPI Intensity
Distance to Max. DAPI
Distance From Pole

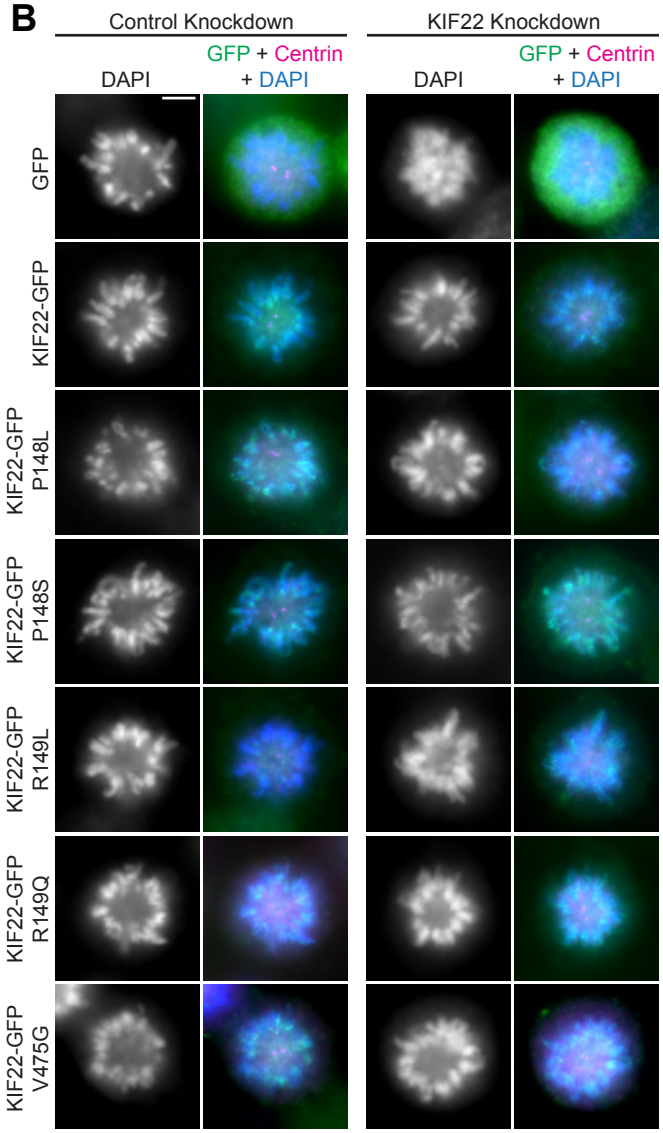
B
Control Knockdown
KIF22 Knockdown
DAPI
GFP + Centrin + DAPI
GFP
KIF22-GFP
KIF22-GFP P148L
KIF22-GFP P148S
KIF22-GFP R149L
KIF22-GFP R149Q
KIF22-GFP V475G

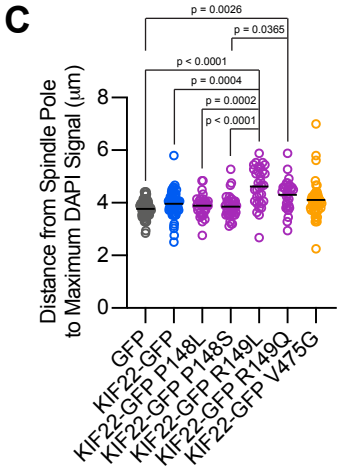
C
Distance from Spindle Pole to Maximum DAPI Signal (µm)
0
2
4
6
8
p = 0.0026
p = 0.0365
p < 0.0001
p = 0.0004
p = 0.0002
p < 0.0001
GFP
KIF22-GFP
KIF22-GFP P148L
KIF22-GFP P148S
KIF22-GFP R149L
KIF22-GFP R149Q
KIF22-GFP V475G

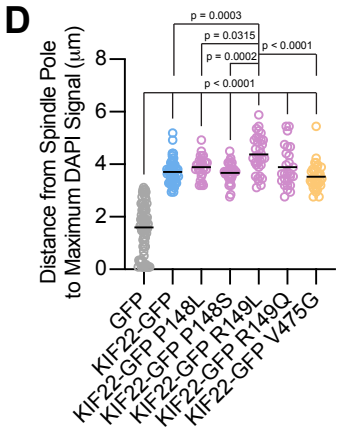
D
Distance from Spindle Pole to Maximum DAPI Signal (µm)
0
2
4
6
8
p = 0.0003
p = 0.0315
p = 0.0002
p < 0.0001
p < 0.0001
GFP
KIF22-GFP
KIF22-GFP P148L
KIF22-GFP P148S
KIF22-GFP R149L
KIF22-GFP R149Q
KIF22-GFP V475G

279 **Figure 3. Pathogenic mutations in KIF22 do not reduce polar ejection forces.**
280 **(A)** Schematic of changes in chromosome positions resulting from loss of polar ejection forces.
281 In cells with monopolar spindles, both spindle poles (magenta) are positioned together and
282 chromosomes (blue) are pushed toward the cell periphery by polar ejection forces (green) (left).
283 In cells depleted of KIF22, polar ejection forces are reduced and chromosomes collapse in toward
284 the center of the cell (right). Relative polar ejection forces were quantified using radial profile plots
285 to measure the distance from the spindle pole to the maximum DAPI signal intensity. **(B)**
286 Immunofluorescence images of monopolar HeLa-Kyoto cells. KIF22-GFP was visualized using
287 an anti-GFP antibody. Fixed approximately 2-3 hours after treatment with monastrol and 24 hours
288 after siRNA transfection and treatment with doxycycline to induce expression. Scale bar 5 μm.
289 Images are representative of 3 or more experiments. **(C)** Distance from the spindle pole to the
290 maximum DAPI signal, a measure of relative polar ejection force level, in cells transfected with
291 control siRNA. 28-69 cells from 3-7 experiments per condition. **(D)** Distance from the spindle pole
292 to the maximum DAPI signal in cells transfected with KIF22 siRNA. 26-75 cells from 3-7
293 experiments per condition. For C-D, bars indicate means. p values from Brown-Forsythe and
294 Welch ANOVA with Dunnett's T3 multiple comparisons test. p values are greater than 0.05 for
295 comparisons without a marked p value.

296 **KIF22 mutations disrupt anaphase chromosome segregation**

297 While pathogenic mutations did not disrupt the function of KIF22 in prometa- or
298 metaphase, HeLa-Kyoto cells expressing mutant KIF22-GFP exhibited defects in anaphase
299 chromosome segregation. In these cells, chromosomes did not move persistently towards the
300 spindle poles. Instead, chromosomes began to segregate, but then reversed direction and moved
301 back towards the center of the spindle or remained in the center of the spindle until
302 decondensation **(Figure 4A).** This phenotype was dominant and occurred in the presence of
303 endogenous KIF22. Recongression was quantified by measuring the distance between
304 separating chromosome masses as anaphase progressed. In cells expressing wild type KIF22-
305 GFP, this value increases steadily and then plateaus. Expression of mutant KIF22-GFP causes
306 the distance between chromosome masses to increase, then decrease as chromosomes
307 recongress, and then increase again as segregation continues **(Figure 4B)**. Recongression
308 reduces the distance between chromosome masses 7 minutes after anaphase onset in cells
309 expressing KIF22-GFP with pathogenic mutations (median distance 2.0 – 7.2 μm) compared to
310 cells expressing wild type KIF22-GFP (median distance 12.9 μm) **(Figure 4C)**. Defects in
311 anaphase chromosome segregation were also observed in RPE-1 cells expressing KIF22-GFP
312 R149Q or V475G **(Figure S3D, S3E, S3F)**. This phenotype is consistent with a lack of KIF22
313 inactivation in anaphase, resulting in a failure to suspend polar ejection force generation.

314 If recongression is the result of increased KIF22 activity in anaphase, we would predict
315 that increased levels of KIF22-GFP expression would cause more severe anaphase chromosome
316 segregation defects. Indeed, plotting the distance between chromosome masses 7 minutes after
317 anaphase onset against mean GFP intensity for each HeLa-Kyoto cell demonstrated that these
318 two values were correlated (Spearman correlation coefficient -0.6246, one-tailed p value <
319 0.0001) **(Figure S3A)**. Considering only cells expressing lower levels of KIF22-GFP (mean
320 background subtracted intensity <100 arbitrary units) emphasized the differences in the distance
321 between chromosome masses as anaphase progressed between cells expressing wild type and
322 mutant motor **(Figure S3B, S3C)**.

323 In a subset of HeLa-Kyoto cells, expression of KIF22-GFP with pathogenic mutations
324 caused cytokinesis failure **(Figure 4D)**. In these cells, cleavage furrow ingression began, but did
325 not complete, resulting in a single daughter cell. The percentage of cells failing to complete
326 cytokinesis was approximately ten-fold higher in cells expressing mutant KIF22-GFP (R149Q
327 36%, V475G 25%) than in cells expressing wild type KIF22-GFP (3%). Additionally, the distance
328 between chromosome masses at the time of cleavage furrow ingression was reduced in cells
329 expressing KIF22-GFP R149Q or V475G, suggesting that the position of the chromosome

330 masses may be physically obstructing cytokinesis **(Figure 4E)**. Consistent with this hypothesis,
331 cells that failed to complete cytokinesis tended to have lower distances between chromosome
332 masses than the distances measured in cells in which cytokinesis completed despite expression
333 of mutant KIF22-GFP **(Figure 4E)**.

Figure 4

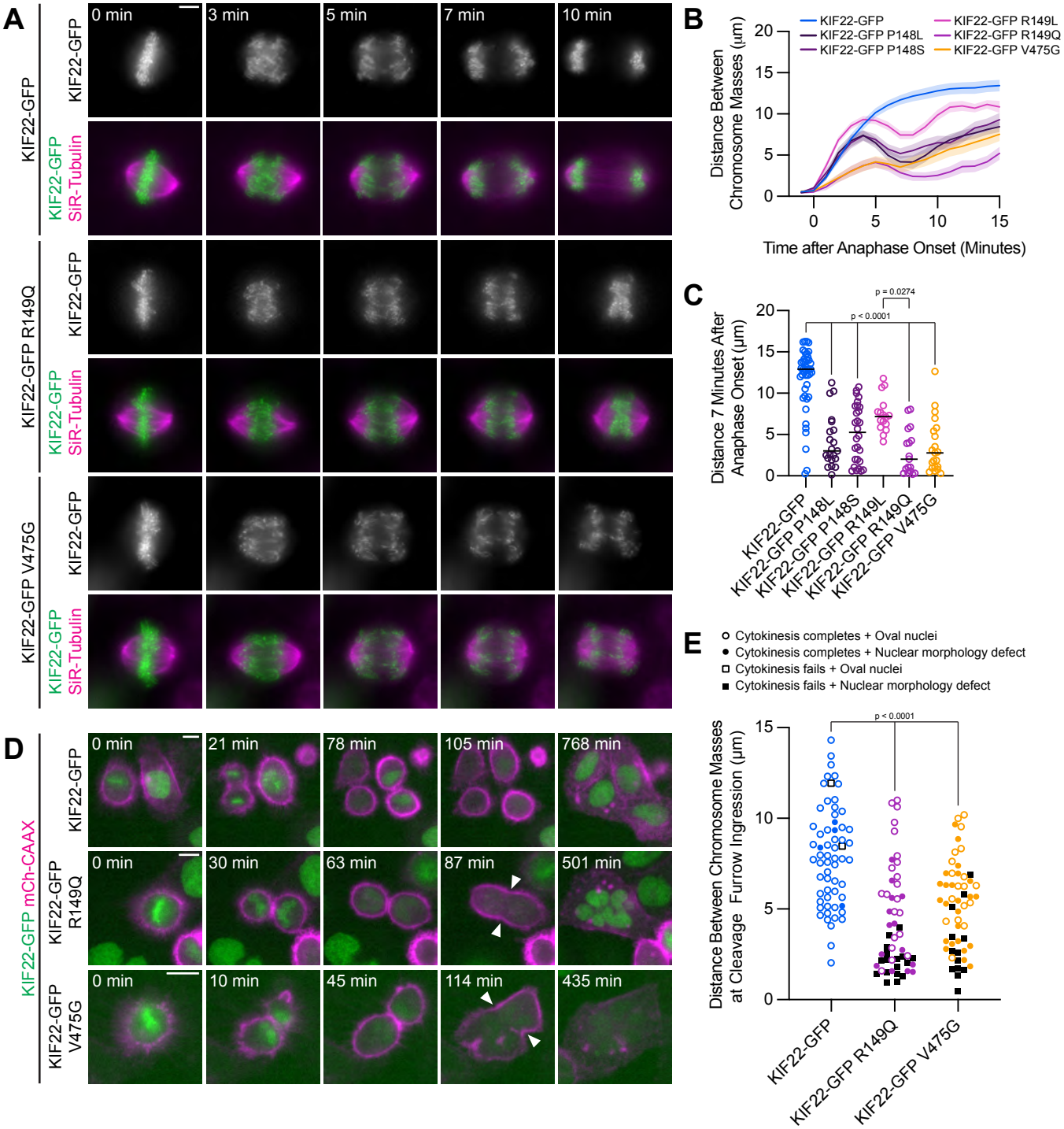
A
KIF22-GFP
KIF22-GFP R149Q
KIF22-GFP V475G
KIF22-GFP
KIF22-GFP
SiR-Tubulin
0 min
3 min
5 min
7 min
10 min
B
KIF22-GFP
KIF22-GFP P148L
KIF22-GFP P148S
KIF22-GFP R149L
KIF22-GFP R149Q
KIF22-GFP V475G
Distance Between Chromosome Masses (µm)
Time after Anaphase Onset (Minutes)
C
p = 0.0274
p < 0.0001
Distance 7 Minutes After Anaphase Onset (µm)
KIF22-GFP
KIF22-GFP P148L
KIF22-GFP P148S
KIF22-GFP R149L
KIF22-GFP R149Q
KIF22-GFP V475G
D
KIF22-GFP mCh-CAAX
KIF22-GFP
KIF22-GFP R149Q
KIF22-GFP V475G
0 min
21 min
78 min
105 min
768 min
30 min
63 min
87 min
501 min
10 min
45 min
114 min
435 min
E
Cytokinesis completes + Oval nuclei
Cytokinesis completes + Nuclear morphology defect
Cytokinesis fails + Oval nuclei
Cytokinesis fails + Nuclear morphology defect
p < 0.0001
Distance Between Chromosome Masses at Cleavage Furrow Ingression (µm)
KIF22-GFP
KIF22-GFP R149Q
KIF22-GFP V475G

334 **Figure 4. Pathogenic mutations in KIF22 disrupt anaphase chromosome segregation.**
335 **(A)** Time-lapse images of dividing HeLa-Kyoto cells expressing KIF22-GFP R149Q or KIF22-GFP
336 V475G. Times indicate minutes after anaphase onset. Images are maximum intensity projections
337 in z through the entirety of the spindle. Imaged approximately 18 hours after treatment with
338 doxycycline to induce expression. Scale bar 5 μm. Images are representative of 3 or more
339 experiments. **(B)** Distance between separating chromosome masses throughout anaphase in
340 HeLa-Kyoto cells. Lines represent the mean and the shaded area denotes SEM. 16-43 cells from
341 4-10 experiments per condition. **(C)** Distance between separating chromosome masses 7 minutes
342 after anaphase onset. Bars indicate medians. p values from Kruskal-Wallis test. p values are
343 greater than 0.05 for comparisons without a marked p value. 16-43 cells from 4-10 experiments
344 per condition. **(D)** Time-lapse images of dividing HeLa-Kyoto cells expressing mCherry (mCh)-
345 CAAX to visualize cell boundaries. Times indicate minutes after anaphase onset. Arrowheads
346 indicate cytokinesis failure. Imaged approximately 8 hours after treatment with doxycycline to
347 induce expression and 24-32 hours after transfection with mCh-CAAX. Scale bars 20 μm. Images
348 are representative of 3 or more experiments. **(E)** Distance between chromosome masses at the
349 time of cleavage furrow ingression. p values from Kruskal-Wallis test. p values are greater than
350 0.05 for comparisons without a marked p value. 52-62 cells from 9-10 experiments per condition.

Supplemental Figure 3

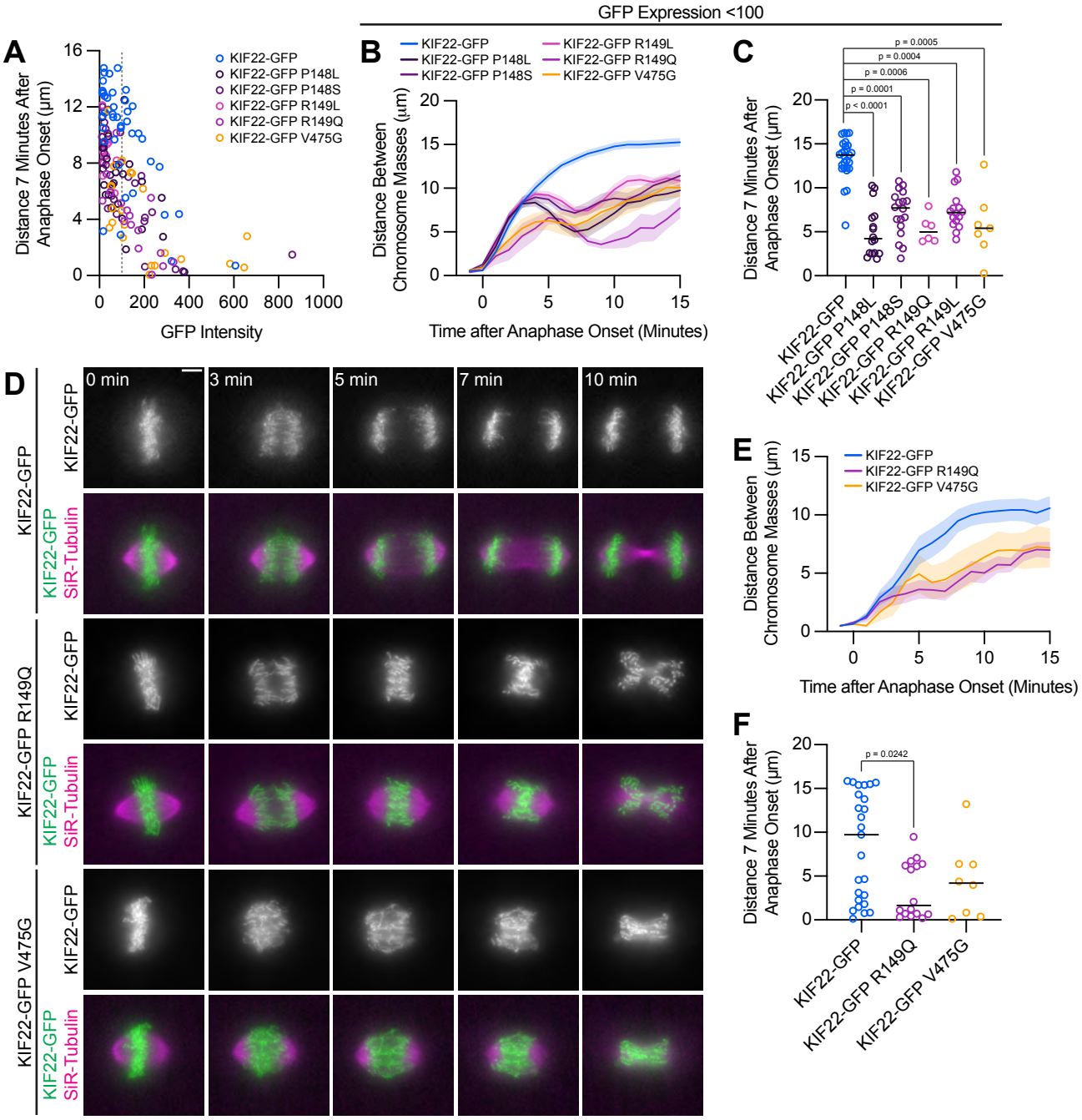

351 **Supplemental Figure 3. Anaphase recongression defects are KIF22-GFP expression level**
352 **dependent and disrupt chromosome segregation in RPE1 cells.**
353 **(A)** Background-subtracted GFP intensity plotted against the distance between separating
354 chromosome masses at 7 minutes to assess dependence of recongression on expression level
355 (Spearman correlation coefficient -0.6246, one-tailed p value < 0.0001). Grey dashed line
356 indicates mean background subtracted GFP intensity of 100. 16-43 cells from 4-10 experiments
357 per condition. **(B)** Distance between separating chromosome masses of cells expressing lower
358 levels of KIF22-GFP (mean background subtracted GFP intensity less than 100). Lines represent
359 the mean and the shaded area denotes SEM. 6-24 cells from 3-8 experiments per condition. **(C)**
360 Distance between separating chromosome masses 7 minutes after anaphase onset of cells
361 expressing lower levels of KIF22-GFP (mean background subtracted GFP intensity less than
362 100). Bars indicate medians. p values from Kruskal-Wallis test. p values are greater than 0.05 for
363 comparisons without a marked p value. 6-24 cells from 3-8 experiments per condition. **(D)** Time-
364 lapse images of dividing RPE-1 cells expressing KIF22-GFP R149Q or KIF22-GFP V475G.
365 Imaged approximately 12-18 hours after treatment with doxycycline to induce expression. Times
366 indicate minutes after anaphase onset. Images are maximum intensity projections in z through
367 the entirety of the spindle. Scale bar 5 μm. Images are representative of 3 or more experiments.
368 **(E)** Distance between separating chromosome masses throughout anaphase in RPE-1 cells.
369 Lines represent the mean and the shaded area denotes SEM. 8-25 cells from 6-7 experiments
370 per condition. **(F)** Distance between separating chromosome masses 7 minutes after anaphase
371 onset in RPE-1 cells. Bars indicate medians. p value from Kruskal-Wallis test. p values are greater
372 than 0.05 for comparisons without a marked p value. 8-25 cells from 6-7 experiments per
373 condition.

374 **Mutations disrupt the separation of the spindle poles in anaphase**

375 Anaphase chromosome segregation requires both that chromosomes move towards the
376 spindle poles (anaphase A) and that the spindle poles move away from one another (anaphase
377 B) (Ris, 1949). To test whether the activity of mutant KIF22 in anaphase affects one or both of
378 these processes, anaphase was imaged in HeLa-Kyoto cells expressing fluorescent markers for
379 the poles (pericentrin-RFP) and centromeres (CENPB-mCh) **(Figure 5A)**. The reduced distance
380 between separating chromosome masses seen in these cells **(Figure 5B, 5C)** was compared to
381 the distances between the centromeres **(Figure 5D, 5E)** and the distances between the poles
382 **(Figure 5F, 5G)** as anaphase progressed. The distances between all three structures showed the
383 same trend: in cells expressing wild type KIF22-GFP, the distance between chromosome masses,
384 between centromeres, and between the spindle poles increased throughout the measured time
385 interval in anaphase. Pathogenic mutations altered the movements of all three structures **(Figure**
386 **5B, 5D, 5F)**. The distance between chromosome masses, between centromeres, and between
387 the spindle poles 10 minutes after anaphase onset was significantly reduced in cells expressing
388 KIF22-GFP R149Q **(Figure 5C, 5E, 5G)**. In cells expressing KIF22-GFP V475G, the same trend
389 was observed, but the reductions in distance were not statistically significant. This suggests that
390 pathogenic mutations in KIF22 disrupt anaphase chromosome segregation by reducing both
391 chromosome segregation to the poles (anaphase A) and spindle pole separation (anaphase B).
392 Comparing the distance between chromosome masses and the spindle pole within each half
393 spindle **(Figure 5H)** with the distance between centromeres and the spindle pole in the same half
394 spindles **(Figure 5I)** demonstrated that expression of mutant KIF22 more potently reduced the
395 segregation of chromosome arms than centromeres, consistent with continued generation of polar
396 ejection forces in anaphase.

Figure 5

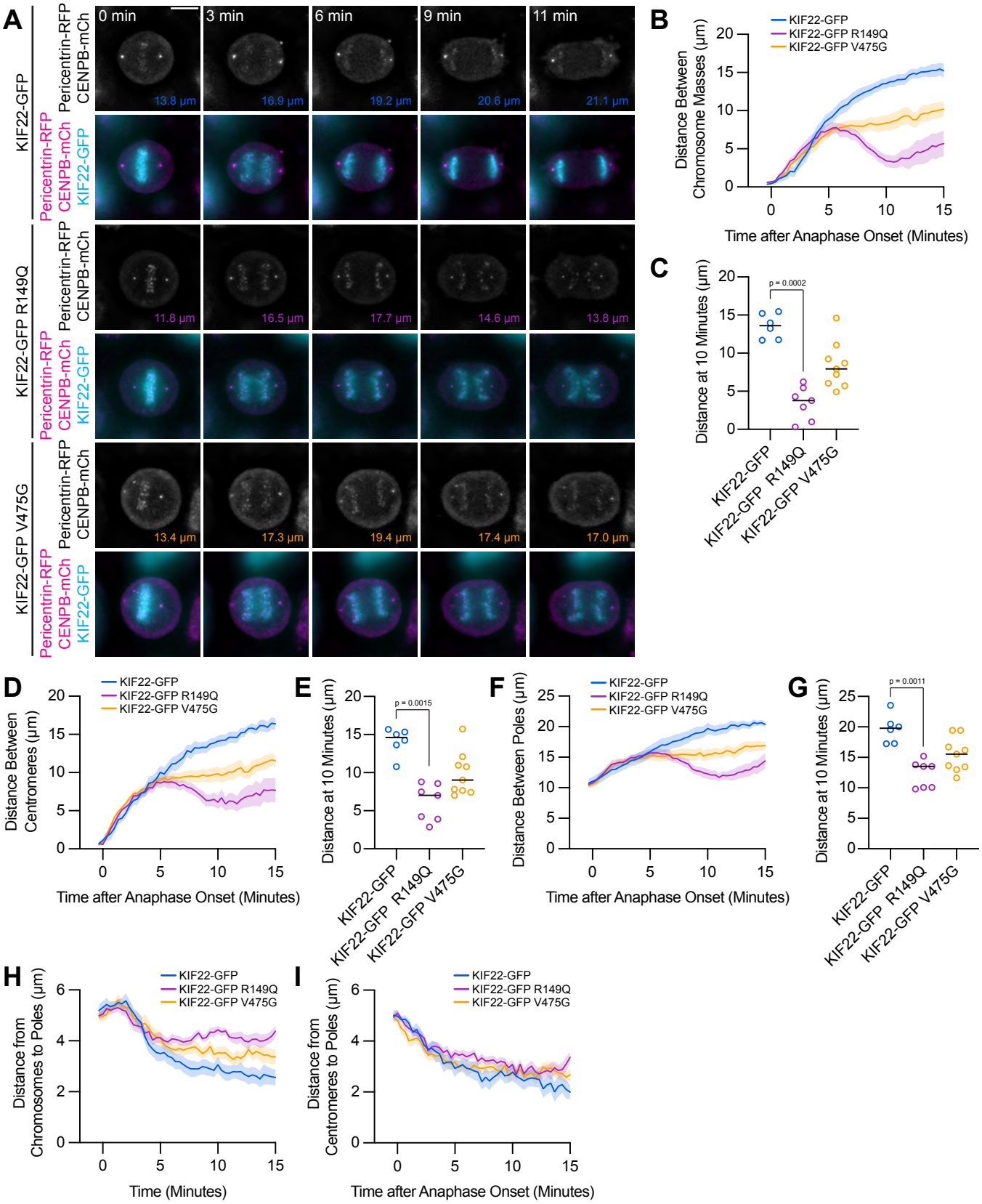
A
KIF22-GFP
KIF22-GFP R149Q
KIF22-GFP V475G
Pericentrin-RFP
CENPB-mCh
KIF22-GFP
0 min
3 min
6 min
9 min
11 min
13.8 µm
16.9 µm
19.2 µm
20.6 µm
21.1 µm
11.8 µm
16.5 µm
17.7 µm
14.6 µm
13.8 µm
13.4 µm
17.3 µm
19.4 µm
17.4 µm
17.0 µm
B
KIF22-GFP
KIF22-GFP R149Q
KIF22-GFP V475G
Distance Between Chromosome Masses (µm)
Time after Anaphase Onset (Minutes)
C
p = 0.0002
Distance at 10 Minutes (µm)
KIF22-GFP
KIF22-GFP R149Q
KIF22-GFP V475G
D
Distance Between Centromeres (µm)
Time after Anaphase Onset (Minutes)
E
p = 0.0015
Distance at 10 Minutes (µm)
F
Distance Between Poles (µm)
Time after Anaphase Onset (Minutes)
G
p = 0.0011
Distance at 10 Minutes (µm)
H
Distance from Chromosomes to Poles (µm)
Time (Minutes)
I
Distance from Centromeres to Poles (µm)
Time after Anaphase Onset (Minutes)

397 **Figure 5. Mutations disrupt the separation of spindle poles in anaphase.**
398 **(A)** Time-lapse images of dividing HeLa-Kyoto cells expressing pericentrin-RFP to mark the
399 spindle poles and CENPB-mCh to mark centromeres. Times indicate minutes after anaphase
400 onset. Colored distances in the bottom right of each greyscale image indicate the distance
401 between the spindle poles in the image. Images are maximum intensity projections in z through
402 the entirety of the spindle. Imaged approximately 24 hours after transfection and 12-18 hours after
403 treatment with doxycycline to induce expression. Images depicting pericentrin-RFP and CENPB-
404 mCh signal were background subtracted by duplicating each frame, applying a gaussian blur
405 (sigma 30 pixels), and subtracting this blurred image from the original. Scale bar 10 μm. Images
406 are representative of 3 or more experiments. **(B)** Distance between separating chromosome
407 masses throughout anaphase in HeLa-Kyoto cells. Lines represent the mean and the shaded
408 area denotes SEM. **(C)** Distance between separating chromosome masses 10 minutes after
409 anaphase onset in HeLa-Kyoto cells. Bars indicate medians. **(D)** Distance between centromeres
410 (CENPB-mCh) throughout anaphase in HeLa-Kyoto cells. Lines represent the mean and the
411 shaded area denotes SEM. **(E)** Distance between centromeres 10 minutes after anaphase onset
412 in HeLa-Kyoto cells. Bars indicate medians. **(F)** Distance between spindle poles (pericentrin-RFP)
413 throughout anaphase in HeLa-Kyoto cells. Lines represent the mean and the shaded area
414 denotes SEM. **(G)** Distance between spindle poles 10 minutes after anaphase onset in HeLa-
415 Kyoto cells. Bars indicate medians. Measurements from the same cells (6-9 cells from 3
416 experiments per condition) are shown in B-G. For C, E, and G, p values from Kruskal-Wallis test.
417 p values are greater than 0.05 for comparisons without a marked p value. **(H)** Distance between
418 chromosome masses and spindle poles throughout anaphase in HeLa-Kyoto cells. Lines
419 represent the mean and the shaded area denotes SEM. **(I)** Distance between centromeres and
420 spindle poles throughout anaphase in HeLa-Kyoto cells. Lines represent the mean and the
421 shaded area denotes SEM. Measurements from the same cells (12-18 half-spindle
422 measurements from 3 experiments per condition) as in B-G are shown in H and I.

423 **Division of cells expressing KIF22 with pathogenic mutations results in daughter cells with**
424 **abnormally shaped nuclei**

425 To understand the consequences of the observed defects in anaphase chromosome
426 segregation, we examined the daughter cells produced by the division of cells expressing KIF22-
427 GFP with pathogenic mutations. In these cells, the nuclei are lobed and fragmented **(Figure 6A)**.
428 The percentage of divisions resulting in nuclear morphology defects was approximately ten-fold
429 higher than in control cells (KIF22-GFP 6%, KIF22-GFP R149Q 64%, KIF22-GFP V475G 68%)
430 when live divisions were observed **(Figure 4E)**. To further quantify this phenotype, the solidity of
431 fixed cell nuclei (the ratio of the area of each nucleus to the area of the convex shape that would
432 enclose it) was measured. A perfectly oval nucleus would have a solidity value of one. Solidity
433 values were reduced in cells expressing KIF22-GFP with pathogenic mutations **(Figure 6B)**,
434 indicating that these cells had more irregularly shaped nuclei. This reduction in solidity was
435 dominant, and occurred both in the presence of endogenous KIF22 and when endogenous KIF22
436 was depleted via siRNA knockdown. Using the fifth percentile solidity of control cells (control
437 knockdown, GFP expression) as a cut-off, 44-63% of cells expressing mutant KIF22-GFP had
438 abnormally shaped nuclei 24 hours after treatment with doxycycline to induce expression of
439 KIF22-GFP **(Figure 6C)**. Expression of wild type KIF22-GFP also resulted in a small increase in
440 the percentage of cells with abnormally shaped nuclei (12%). This percentage was reduced when
441 endogenous KIF22 was depleted (7%), consistent with nuclear morphology defects resulting from
442 an increase in KIF22 activity.

443 Expression of KIF22-GFP with pathogenic mutations also caused abnormally shaped
444 nuclei in RPE-1 cells **(Figure S4A)**. The solidity of nuclei in cells expressing mutant KIF22-GFP
445 was reduced **(Figure S4B)**, and 40-49% of RPE-1 cells expressing mutant KIF22-GFP had
446 abnormally shaped nuclei, again defined as a solidity value less than the fifth percentile of control
447 cells **(Figure 4C)**. In RPE-1 cells, expression of wild type KIF22-GFP resulted in a higher
448 percentage of cells with abnormally shaped nuclei (18% in control knockdown cells, 15% with
449 KIF22 knockdown) than was seen in HeLa-Kyoto cells. This may be a result of the higher
450 expression level of KIF22-GFP in the RPE-1 inducible cell lines **(Figure S1I, S1K)**.

451 To determine whether these nuclear morphology defects depended on the ability of KIF22
452 to generate forces within the mitotic spindle, cells were treated with nocodazole to depolymerize
453 microtubules and reversine to silence the spindle assembly checkpoint, allowing cells to enter
454 and exit mitosis without assembling a spindle or segregating chromosomes (Samwer et al., 2017;
455 Serra-Marques et al., 2020) **(Figure 6D)**. The solidity of nuclei was measured before
456 chromosomes condensed **(Figure 6E)** and after mitotic exit **(Figure 6F)**. At both time points, there

457 was no difference in nuclear shape between control cells and cells expressing KIF22-GFP with
458 pathogenic mutations, indicating that the effects of mutations on nuclear structure are spindle-
459 dependent.

460 The effect of nuclear morphology defects on daughter cell fitness may partially depend on
461 whether the nuclear envelopes of abnormally shaped nuclei are intact. The expression of mCherry
462 (mCh) with a nuclear localization signal (NLS) indicated that even highly lobed and fragmented
463 nuclei in cells expressing mutant KIF22-GFP are capable of retaining nuclear-localized proteins
464 **(Figure 6G)**. This suggests that the nuclear envelopes of these abnormally shaped nuclei are still
465 intact enough to function as a permeability barrier (Hatch, Fischer, Deerinck, & Hetzer, 2013).

Figure 6

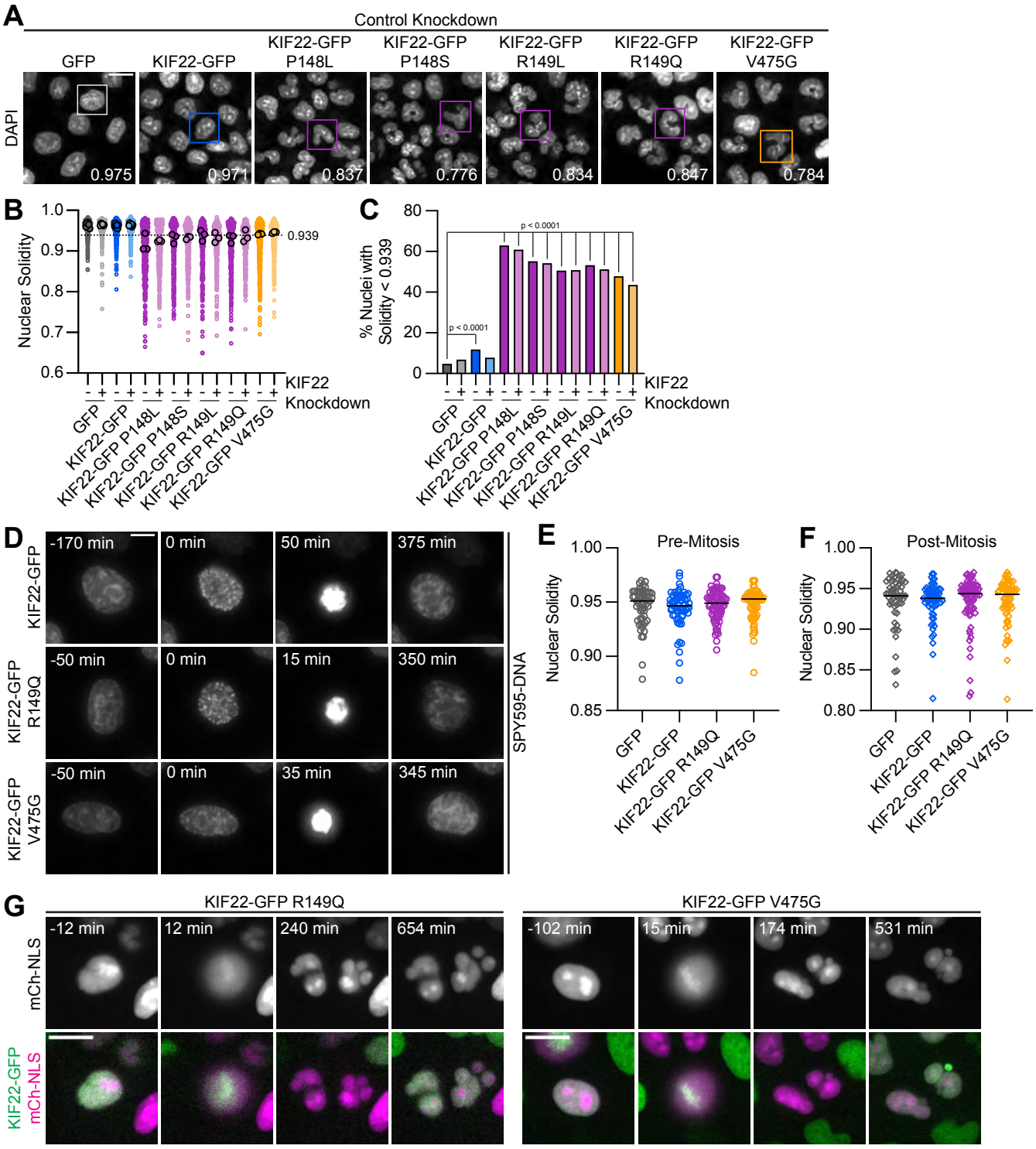
A
Control Knockdown
GFP
KIF22-GFP
KIF22-GFP P148L
KIF22-GFP P148S
KIF22-GFP R149L
KIF22-GFP R149Q
KIF22-GFP V475G
DAPI
0.975
0.971
0.837
0.776
0.834
0.847
0.784
B
Nuclear Solidity
1.0
0.9
0.8
0.7
0.6
0.939
KIF22 Knockdown
C
% Nuclei with Solidity < 0.939
80
60
40
20
0
p < 0.0001
p < 0.0001
D
KIF22-GFP
-170 min
0 min
50 min
375 min
KIF22-GFP R149Q
-50 min
0 min
15 min
350 min
KIF22-GFP V475G
-50 min
0 min
35 min
345 min
SPY595-DNA
E
Pre-Mitosis
Nuclear Solidity
1.00
0.95
0.90
0.85
F
Post-Mitosis
Nuclear Solidity
1.00
0.95
0.90
0.85
0.80
G
KIF22-GFP R149Q
KIF22-GFP V475G
mCh-NLS
-12 min
12 min
240 min
654 min
-102 min
15 min
174 min
531 min
KIF22-GFP
mCh-NLS

466 **Figure 6. Division of cells expressing KIF22 with pathogenic mutations results in daughter**
467 **cells with abnormally shaped nuclei.**
468 **(A)** DAPI stained nuclei of cells expressing KIF22 with pathogenic mutations. Values in the bottom
469 right of each image indicate the solidity of the boxed nucleus. Fixed approximately 24 hours after
470 treatment with doxycycline to induce expression. Scale bar 20 μm. Images are representative of
471 3 or more experiments. **(B)** Measured solidity of nuclei in HeLa-Kyoto cell lines. Small circles
472 represent the solidity of individual nuclei, and large circles with black outlines indicate the median
473 of each experiment. A dashed line marks a solidity value of 0.939, the fifth percentile of solidity
474 for control cells transfected with control siRNA and expressing GFP. **(C)** Percentage of nuclei with
475 abnormal shape, indicated by a solidity value less than 0.939, the fifth percentile of control (control
476 knockdown, GFP expression) cell solidity. A chi-square test of all data produced a p value <
477 0.0001. Plotted p values are from pairwise post-hoc chi-square tests comparing control (control
478 knockdown, GFP expression) cells to each other condition. Applying the Bonferroni correction for
479 multiple comparisons, a p value of less than 0.00385 was considered significant. p values are
480 greater than 0.00385 for comparisons without a marked p value. Data in (B) and (C) represent
481 336-1045 cells from 3-6 experiments per condition. **(D)** Time-lapse images of HeLa-Kyoto cells
482 treated with nocodazole and reversine and stained with SPY595-DNA to visualize chromosomes.
483 Time indicates the number of minutes before or after chromosome condensation. Images are
484 maximum intensity projections in z of two focal planes, one at the level of interphase nuclei and
485 one at the level of mitotic chromosomes. Imaged approximately 8 hours after treatment with
486 doxycycline to induce expression, 1.5-2 hours after treatment with SPY595-DNA, and 0.5-1 hour
487 after treatment with nocodazole and reversine. Scale bar 10 μm. Images are representative of 3
488 or more experiments. **(E)** Nuclear solidity of HeLa-Kyoto cells treated with nocodazole and
489 reversine. Measurements were made 15 minutes before chromosome condensation. **(F)** Nuclear
490 solidity of HeLa-Kyoto cells treated with nocodazole and reversine. Measurements were made
491 100 minutes after chromosome decondensation. Data in (E) and (F) represent 56-76 cells from 3
492 experiments per condition. For (E) and (F), bars indicate medians, and the Kruskal-Wallis test
493 indicated no significant difference between groups. **(G)** Time-lapse images of HeLa-Kyoto cells
494 expressing mCherry (mCh)-NLS to assess nuclear envelope integrity. Times indicate minutes
495 before or after chromosome condensation. Imaged approximately 8 hours after treatment with
496 doxycycline to induce expression and 24 hours after transfection with mCh-CAAX. Scale bar 20
497 μm. Images are representative of 3 or more experiments.

Supplemental Figure 4

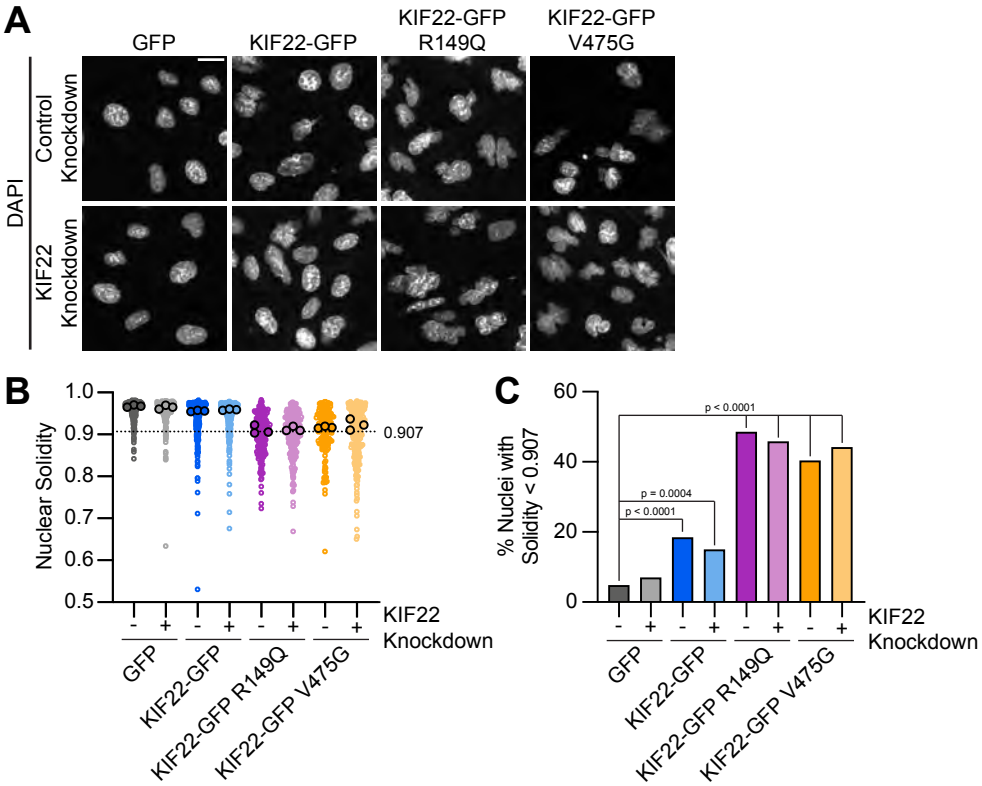

498 **Supplemental Figure 4. Mutations cause abnormally shaped nuclei in RPE1 cells.**
499 **(A)** DAPI-stained nuclei of RPE-1 cells expressing KIF22-GFP with pathogenic mutations. Fixed
500 approximately 24 hours after treatment with doxycycline to induce expression. Scale bar 20 μm.
501 Images are representative of 3 or more experiments. **(B)** Measured solidity of nuclei in RPE-1 cell
502 lines. Small circles represent the solidity of individual nuclei, and large circles with black outlines
503 indicate the median of each experiment. A dashed line marks a solidity value of 0.907, the fifth
504 percentile of solidity for control cells transfected with control siRNA and expressing GFP. **(C)**
505 Percentage of nuclei with abnormal shape, indicated by a solidity value less than 0.907, the fifth
506 percentile of control (control knockdown, GFP expression) cell solidity. A chi-square test of all
507 data produced a p value < 0.0001. Plotted p values are from pairwise post-hoc chi-square tests
508 comparing control (control knockdown, GFP expression) cells to each other condition. Applying
509 the Bonferroni correction for multiple comparisons, a p value of less than 0.00714 was considered
510 significant. p values are greater than 0.00714 for comparisons without a marked p value. Data in
511 (B) and (C) represent 146-244 cells from 3 experiments per condition.

512 **Proliferation is reduced in cells expressing KIF22 with pathogenic mutations**

513 If defects in anaphase chromosome segregation and nuclear morphology affect cellular
514 function, they may impact the ability of cells to proliferate. To test this, HeLa-Kyoto cells
515 expressing KIF22-GFP with pathogenic mutations were imaged over 96 hours to count the
516 numbers of cells over time **(Figure 7A)**. The growth rates of cells expressing mutant KIF22 were
517 reduced **(Figure 7B)**. After 96 hours, the fold change in cell number was reduced by
518 approximately 30% for cells expressing KIF22-GFP with pathogenic mutations (GFP control
519 median 5.3, KIF22-GFP R149Q 3.7, KIF22-GFP V475G 3.8) **(Figure 7C)**.

520 To consider what might be limiting the proliferation rate of cells expressing mutant KIF22-
521 GFP, predictions for proliferation rate based on the observed rates of nuclear morphology defects
522 and cytokinesis failure were calculated. For these purposes, only data from the first 48 hours of
523 the proliferation assay were used, as cell growth rates plateaued after this timepoint. The doubling
524 time of control HeLa-Kyoto cells expressing GFP was calculated to be 20.72 hours in these
525 experiments, which is consistent with published data (Y. Liu et al., 2018). Using this doubling rate,
526 assuming exponential growth, and assuming every cell divides, the normalized cell count at 48
527 hours (normalized to a starting cell count of 1) was predicted to be 4.98. This is close to the
528 experimental 48-hour cell count for control cells (4.60), and higher than the experimental 48-hour
529 cell count for cells expressing KIF22-GFP R149Q (3.13) or V475G (3.60), as these cell lines have
530 reduced proliferation **(Figure 7B, square)**. If one assumed that cells with abnormally shaped
531 nuclei stop dividing, given that approximately 60% of mutant KIF22-GFP cell divisions result in
532 abnormally shaped nuclei **(Figure 4E),** the predicted cell count at 48 hours would be 2.18 **(Figure**
533 **7B, triangle)**. This is lower than the experimental cell count for cells expressing mutant KIF22-
534 GFP, suggesting that cells with abnormally shaped nuclei must be capable of additional divisions.
535 If, instead, one assumed that only cells that fail cytokinesis (30% of cells **(Figure 4E)**) stop
536 dividing, the predicted cell count would be 3.42 **(Figure 7B, diamond)**. This value is consistent
537 with the experimental 48-hour cell count for cells expressing KIF22-GFP with pathogenic
538 mutations (3.13 – 3.60), suggesting the rate of cytokinesis failure may limit the rate of proliferation
539 in these cells. Consistent with this possibility, an increased number of large cells that may have
540 failed cytokinesis are visible in proliferation assay images at 72 hours **(Figure 7A)**.

541 To test the prediction that cells with nuclear morphology defects are capable of division,
542 KIF22-GFP expression was induced approximately 24 hours before imaging to generate a
543 population of cells with abnormally shaped nuclei. Division of these cells was observed **(Figure**
544 **7D)**, demonstrating that nuclear morphology defects do not prevent subsequent divisions. The
545 percentage of cells that divided over the course of this experiment was not reduced in cells

546 expressing KIF22-GFP with pathogenic mutations despite the abnormal nuclear morphology of
547 cells in those populations **(Figure 7E)**.

Figure 7

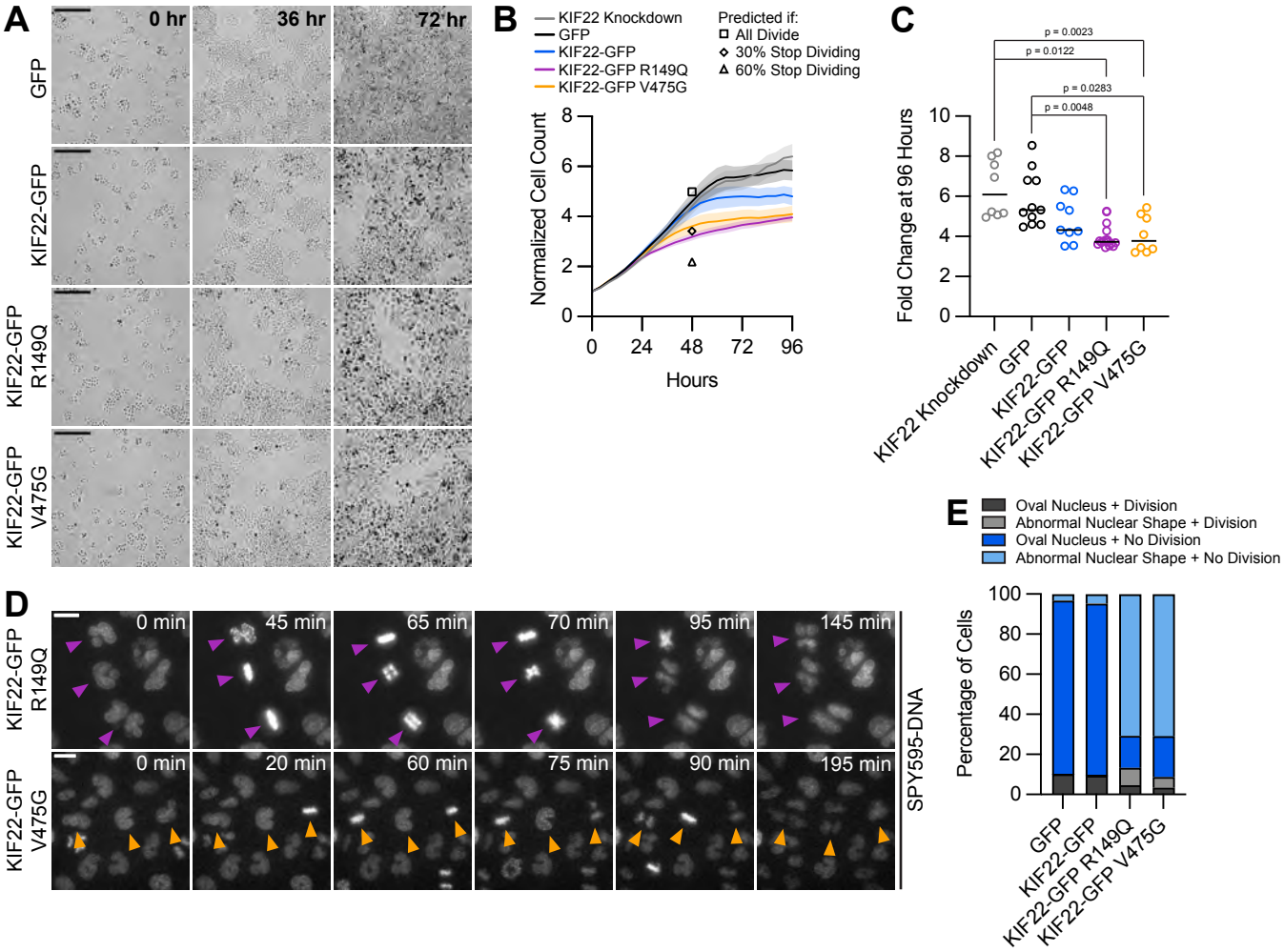
A
0 hr
36 hr
72 hr
GFP
KIF22-GFP
KIF22-GFP R149Q
KIF22-GFP V475G
B
KIF22 Knockdown
GFP
KIF22-GFP
KIF22-GFP R149Q
KIF22-GFP V475G
Predicted if:
All Divide
30% Stop Dividing
60% Stop Dividing
Normalized Cell Count
Hours
C
p = 0.0023
p = 0.0122
p = 0.0283
p = 0.0048
Fold Change at 96 Hours
KIF22 Knockdown
GFP
KIF22-GFP
KIF22-GFP R149Q
KIF22-GFP V475G
D
0 min
45 min
65 min
70 min
95 min
145 min
0 min
20 min
60 min
75 min
90 min
195 min
SPY595-DNA
E
Oval Nucleus + Division
Abnormal Nuclear Shape + Division
Oval Nucleus + No Division
Abnormal Nuclear Shape + No Division
Percentage of Cells
GFP
KIF22-GFP
KIF22-GFP R149Q
KIF22-GFP V475G

548 **Figure 7. Proliferation is reduced in cells expressing KIF22 with pathogenic mutations.**
549 **(A)** Time-lapse bright field images of HeLa-Kyoto cells to assess proliferation rate. Scale bar 500
550 μm. Images are representative of 3 or more experiments. **(B)** Proliferation rates measured using
551 automated bright field imaging. Lines represent the mean cell count, normalized to the number of
552 cells at 0 hours, and the shaded area denotes SEM. Black outlined shapes indicate the predicted
553 cell count for cell lines expressing pathogenic mutations at 48 hours if every cell doubled every
554 20.72 hours (the doubling time measured from 48 hours of control cell proliferation) (square), if
555 the rate of cytokinesis failure limited proliferation and 30% of cells did not divide (diamond), and
556 if the rate of nuclear morphology defects limited proliferation and 60% of cells did not divide
557 (triangle). **(C)** Fold change of normalized cell counts after 96 hours. Bars indicate medians. p
558 values from Kruskal-Wallis test. p values are greater than 0.05 for comparisons without a marked
559 p value. Data in (B) and (C) represent 8-16 technical replicates from 4 experiments per condition.
560 **(D)** Time-lapse imaging of HeLa-Kyoto cells treated with doxycycline for 24 hours to induce
561 expression of KIF22-GFP with pathogenic mutations and stained with SPY595-DNA. Arrowheads
562 indicate cells with abnormally shaped nuclei that divide. Images are maximum intensity
563 projections in z of two focal planes, one at the level of interphase nuclei and one at the level of
564 mitotic chromosomes. Scale bars 20 μm. Images are representative of 3 or more experiments.
565 **(E)** Nuclear morphology at the start of imaging (dark grey or blue, oval; light grey or blue; abnormal
566 morphology) and outcome (grey, cell divides during the experiment; blue, the cell does not divide).
567 The total number of dividing cells was compared between cell lines using the chi-square test ($p <$
568 0.0001 across all conditions). Post-hoc chi-square tests comparing all conditions to one another
569 indicated that the proliferation rate of cells expressing KIF22-GFP R149Q is statistically different
570 than that of cells expressing GFP ($p = 0.0025$), KIF22-GFP ($p = 0.0003$), or KIF22-GFP V475G
571 ($p < 0.0001$). Applying the Bonferroni correction for multiple comparisons, a p value of less than
572 0.008 was considered significant. p values are greater than 0.008 for all other comparisons. 1890-
573 2611 cells from 4 experiments per condition.

574 **Mimicking phosphorylation of T463 phenocopies pathogenic mutations**

575 The phenotypes observed in cells expressing KIF22-GFP with pathogenic mutations
576 suggest that mutations may prevent inactivation of KIF22 in anaphase, and that polar ejection
577 forces in anaphase disrupt chromosome segregation. If this is the case, then preventing KIF22
578 inactivation would be predicted to phenocopy the pathogenic mutations. One mechanism by
579 which KIF22 activity is controlled is phosphorylation of T463: phosphorylation of this tail residue
580 is necessary for polar ejection force generation, and dephosphorylation at anaphase onset
581 contributes to polar ejection force suppression (Soeda et al., 2016). Therefore, we generated
582 HeLa-Kyoto inducible cell lines expressing KIF22-GFP with phosphomimetic (T463D) and
583 phosphonull (T463A) mutations to test whether preventing KIF22 inactivation in anaphase by
584 expressing the constitutively active T463D construct phenocopies the expression of KIF22-GFP
585 with pathogenic mutations. When treated with doxycycline, these cells expressed
586 phosphomimetic and phosphonull KIF22-GFP at levels comparable to those seen in cells lines
587 expressing KIF22-GFP with pathogenic mutations, which was approximately two- to three-fold
588 higher than the level of expression of endogenous KIF22 **(Figure S5A-D)**.

589 To assess the activity of KIF22-GFP T463D and T463A in HeLa cells, polar ejection force
590 generation in monopolar spindles was measured **(Figure 8A)**. In cells with endogenous KIF22
591 present, expression of KIF22-GFP T463D increased the distance from the spindle pole to the
592 maximum DAPI signal (GFP control 3.7 ± 0.07 μm, KIF22-GFP T463D 4.4 ± 0.12, mean ± SEM),
593 indicating increased polar ejection forces, consistent with phosphorylation of T463 activating
594 KIF22 in prometaphase (Soeda et al., 2016) **(Figure 8B)**. Conversely, when endogenous KIF22
595 was depleted, expression of KIF22-GFP T463A was less able to rescue polar ejection force
596 generation (distance from the spindle pole to the maximum DAPI signal 3.0 ± 0.08 μm, mean ±
597 SEM) than expression of wild type KIF22-GFP (3.6 ± 0.07 μm) or KIF22-GFP T463D (3.7 ± 0.10
598 μm) **(Figure 8C)**. Again, this is consistent with previous work demonstrating that KIF22
599 phosphorylation at T463 activates the motor for prometaphase polar ejection force generation
600 (Soeda et al., 2016), although the reduction in polar ejection forces seen with KIF22-GFP T463A
601 rescue is less severe in our system, possibly due to differences in cell type, level of depletion of
602 endogenous KIF22, or the method used to quantify polar ejection forces.

603 In anaphase, expression of phosphomimetic KIF22-GFP T463D, but not phosphonull
604 KIF22-GFP T463A, caused chromosome recongression **(Figure 8D, 8E)**. The distance between
605 chromosome masses at 7 minutes was reduced in cells expressing KIF22-GFP T463D (median
606 5.8 μm) compared to cells expressing wild type KIF22-GFP (12.5 μm) or KIF22-GFP T463A (10.8
607 μm) **(Figure 8F)**. As in cells expressing KIF22-GFP with pathogenic mutations, the severity of

608 anaphase chromosome recongression, indicated by the distance between chromosome masses
609 at 7 minutes, was dependent on GFP expression level (Spearman correlation coefficient -0.3964,
610 one-tailed p value 0.0004) **(Figure S5E)**. When only cells expressing lower levels of KIF22-GFP
611 (mean background subtracted intensity <100 arbitrary units) were considered, the same effect
612 (expression of KIF22-GFP T463D causes recongression) was still observed **(Figure S5F, S5G)**.
613 This recongression phenocopies the effect of pathogenic mutations on anaphase chromosome
614 segregation, consistent with pathogenic mutations preventing anaphase inactivation of KIF22.
615 In addition to causing the same defects in anaphase chromosome segregation, expression
616 of KIF22-GFP T463D also affects daughter cell nuclear morphology. Cells expressing KIF22-GFP
617 T463D have lobed and fragmented nuclei **(Figure S5H)** and correspondingly reduced nuclear
618 solidity measurements **(Figure 8G)**. An increased percentage of cells expressing KIF22-GFP
619 T463D in the presence of endogenous KIF22 (65%) or in cells depleted of endogenous KIF22
620 (72%) have abnormally shaped nuclei, as indicated by a solidity value below the fifth percentile
621 of control cell nuclear solidity **(Figure 8H)**.
622 Expression of KIF22-GFP T463A also resulted in a small increase in the percentage of
623 abnormally shaped nuclei (26% in control or KIF22 knockdown conditions) **(Figure 8H)**. Since
624 expression of KIF22-GFP T463A does not cause anaphase recongression **(Figure 8E)**, the level
625 of compaction of the segregating chromosome masses was explored as a possible explanation
626 for this modest increase in the percentage of cells with nuclear morphology defects. In KIF22
627 knockout mice, loss of KIF22 reduces chromosome compaction in anaphase, causing the
628 formation of multinucleated cells (Ohsugi et al., 2008). The phosphonull T463A mutation reduces
629 KIF22 activity and may therefore exhibit a KIF22 loss of function phenotype. Measurement of the
630 widths of separating chromosome masses in anaphase **(Figure S5I)** did demonstrate a modest
631 broadening of the chromosome masses in cells expressing KIF22-GFP T463A **(Figure S5J,**
632 **S5K)**, which may contribute to the modest defects in nuclear morphology seen in these cells.

Figure 8

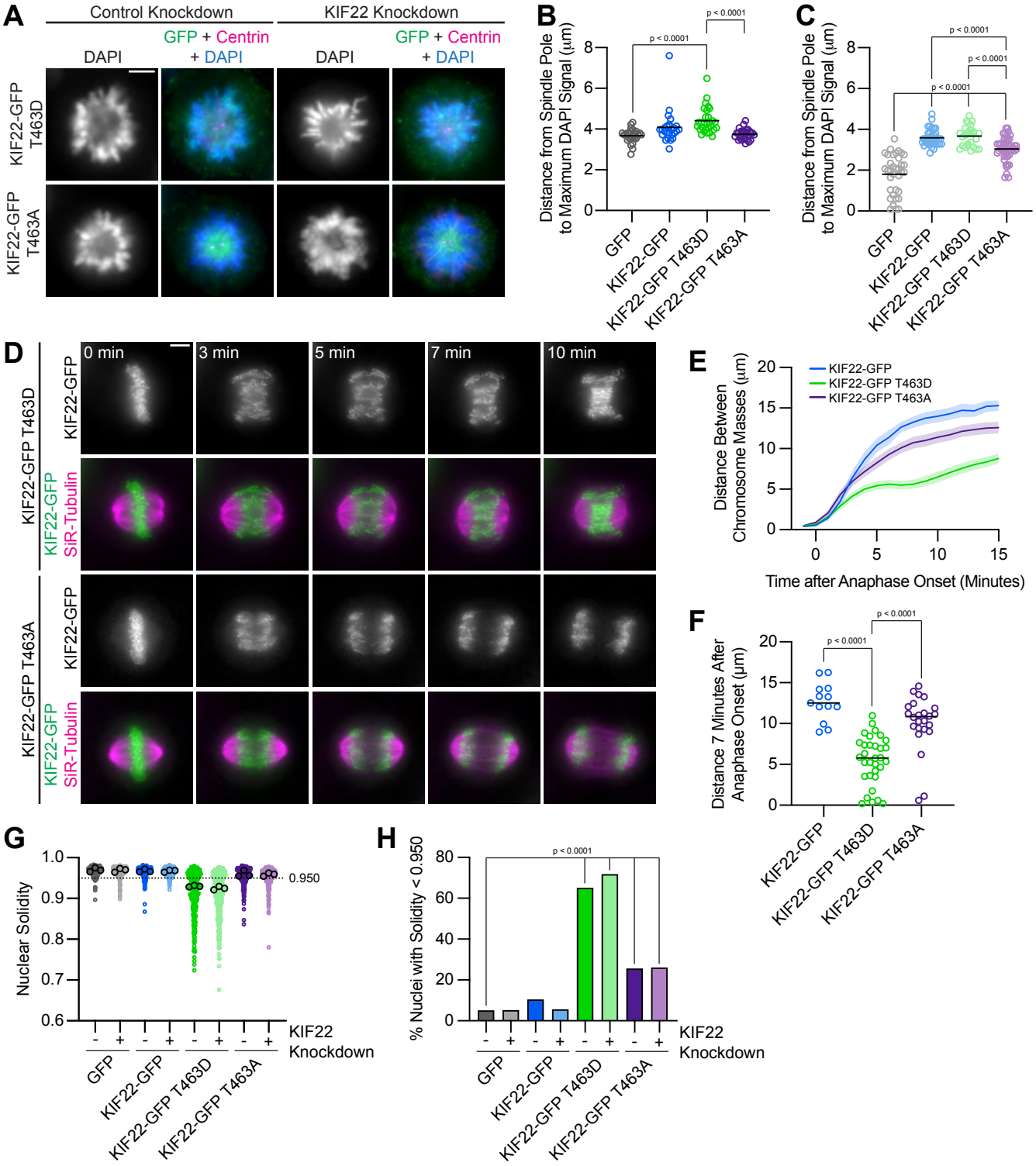
A
Control Knockdown
KIF22 Knockdown
DAPI
GFP + Centrin + DAPI
KIF22-GFP T463D
KIF22-GFP T463A
B
Distance from Spindle Pole to Maximum DAPI Signal (µm)
p < 0.0001
GFP
KIF22-GFP
KIF22-GFP T463D
KIF22-GFP T463A
C
D
0 min
3 min
5 min
7 min
10 min
KIF22-GFP
KIF22-GFP SiR-Tubulin
E
Distance Between Chromosome Masses (µm)
Time after Anaphase Onset (Minutes)
F
Distance 7 Minutes After Anaphase Onset (µm)
G
Nuclear Solidity
0.950
KIF22 Knockdown
H
% Nuclei with Solidity < 0.950

633 **Figure 8. Phosphomimetic mutation of T463 phenocopies pathogenic mutations in KIF22.**
634 **(A)** Immunofluorescence images of monopolar HeLa-Kyoto cells. KIF22-GFP was visualized
635 using an anti-GFP antibody. Fixed approximately 2-3 hours after treatment with monastrol and 24
636 hours after siRNA transfection and treatment with doxycycline to induce expression. Scale bar 5
637 μm. Images are representative of 3 or more experiments. **(B)** Distance from the spindle pole to
638 the maximum DAPI signal, a measure of relative polar ejection force level, between HeLa-Kyoto
639 cell lines expressing KIF22-GFP with phosphomimetic and phosphonull mutations. 26-29 cells
640 from 3 experiments per condition. **(C)** Distance from the spindle pole to the maximum DAPI signal
641 in cells depleted of endogenous KIF22 and expressing KIF22-GFP with phosphomimetic and
642 phosphonull mutations. 27-47 cells from 3-4 experiments per condition. For B-C, bars indicate
643 means. p values from Brown-Forsythe and Welch ANOVA with Dunnett's T3 multiple comparisons
644 test. p values are greater than 0.05 for comparisons without a marked p value. **(D)** Time-lapse
645 images of dividing HeLa-Kyoto cells. Cells expressing KIF22-GFP T463D exhibit recongression
646 of the chromosomes during anaphase. Times indicate minutes after anaphase onset. Images are
647 maximum intensity projections in z through the entirety of the spindle. Imaged approximately 18
648 hours after treatment with doxycycline to induce expression. Scale bar 5 μm. Images are
649 representative of 3 or more experiments. **(E)** Distance between separating chromosome masses
650 throughout anaphase in HeLa-Kyoto cells. Lines represent the mean and the shaded area
651 denotes SEM. 13-32 cells from 5 experiments per condition. **(F)** Distance between separating
652 chromosome masses 7 minutes after anaphase onset. Bars indicate medians. p values from
653 Kruskal-Wallis test. p values are greater than 0.05 for comparisons without a marked p value. 13-
654 32 cells from 5 experiments per condition. **(G)** Measured solidity of nuclei in HeLa-Kyoto cell lines.
655 Small circles represent the solidity of individual nuclei, and large circles with black outlines
656 indicate the median of each experiment. A dashed line marks a solidity value of 0.950, the fifth
657 percentile of solidity for control cells transfected with control siRNA and expressing GFP. **(H)**
658 Percentage of nuclei with abnormal shape, indicated by a solidity value less than 0.950, the fifth
659 percentile of control (control knockdown, GFP expression) cell solidity. A chi-square test of all
660 data produced a p value < 0.0001. Plotted p values are from pairwise post-hoc chi-square tests
661 comparing control (control knockdown, GFP expression) cells to each other condition. Applying
662 the Bonferroni correction for multiple comparisons, a p value of less than 0.00714 was considered
663 significant. p values are greater than 0.00714 for comparisons without a marked p value. Data in
664 (G) and (H) represent 312-376 cells from 3 experiments per condition.

Supplemental Figure 5

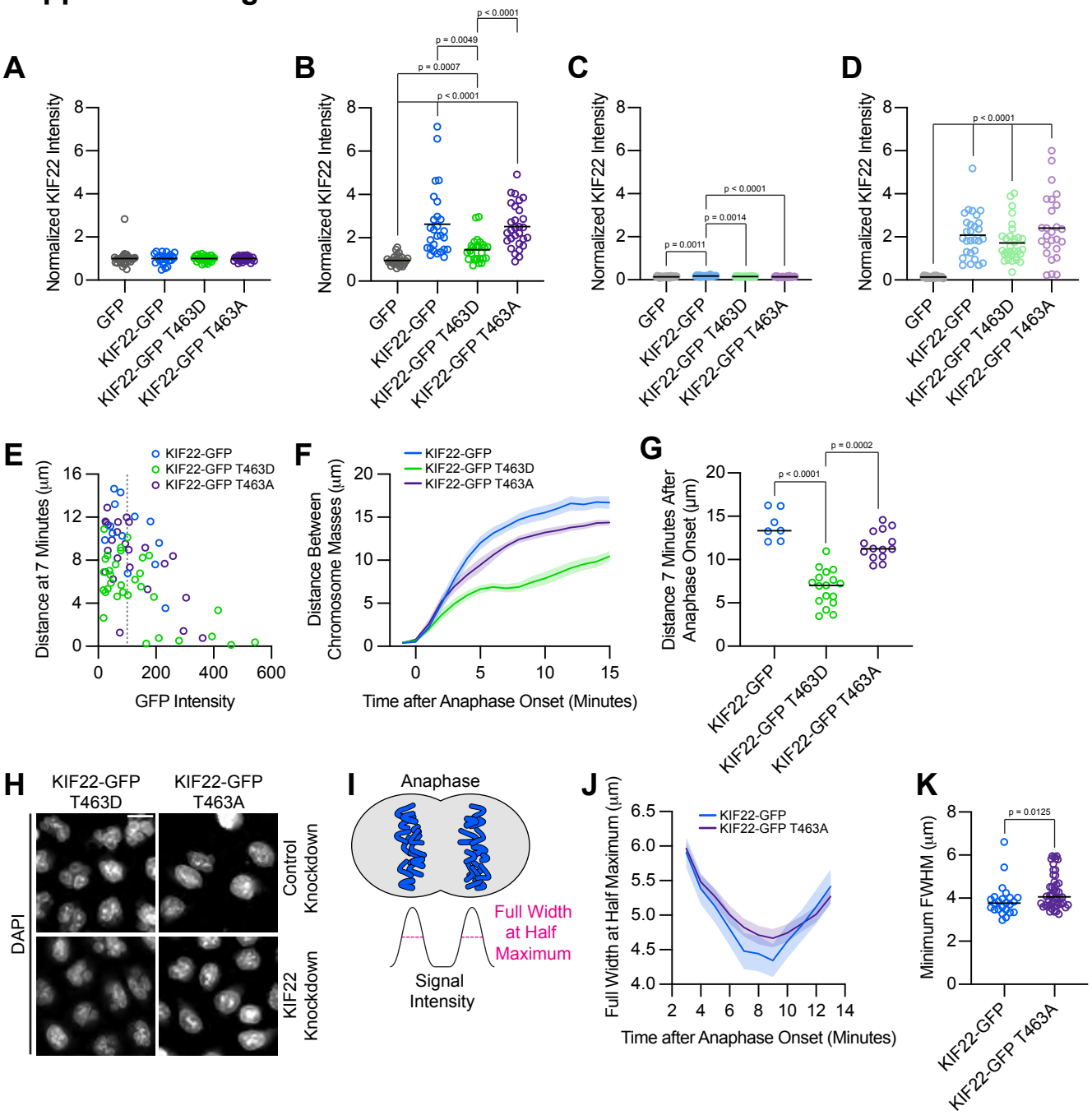

665 **Supplemental Figure 5. Cells expressing KIF22-GFP T463A have broader anaphase**
666 **chromosome masses.**
667 **(A-D)** Quantification of KIF22 fluorescence intensity in untreated HeLa-Kyoto cells transfected
668 with control siRNA (A), cells treated with doxycycline to induce expression and transfected with
669 control siRNA (B), untreated cells transfected with KIF22 siRNA (C), and cells treated with
670 doxycycline and transfected with KIF22 siRNA (D) normalized to the mean intensity of uninduced,
671 control knockdown cells (endogenous KIF22 expression level) for each cell line (A). 23-32 HeLa-
672 Kyoto cells per condition from 3 experiments. **(E)** Plotting background-subtracted GFP intensity
673 against the distance between separating chromosome masses at 7 minutes indicates that this
674 distance is dependent on expression level (Spearman correlation coefficient -0.3964, one-tailed
675 p value = 0.0004). Grey dashed line indicates mean background subtracted GFP intensity of 100.
676 13-32 cells from 5 experiments per condition. **(F)** Distance between separating chromosome
677 masses of cells expressing lower levels of KIF22-GFP (mean background subtracted GFP
678 intensity less than 100). Lines represent the mean and the shaded area denotes SEM. 7-14 cells
679 from 4-5 experiments per condition. **(G)** Distance between separating chromosome masses 7
680 minutes after anaphase onset of cells expressing lower levels of KIF22-GFP (mean background
681 subtracted GFP intensity less than 100). Bars indicate medians. p values from Kruskal-Wallis test.
682 p values are greater than 0.05 for comparisons without a marked p value. 7-14 cells from 4-5
683 experiments per condition. **(H)** DAPI-stained nuclei of Hela-Kyoto cells. Fixed approximately 24
684 hours after treatment with doxycycline to induce expression. Scale bar 20 μm. Images are
685 representative of 3 or more experiments. **(I)** Schematic depicting the measurement of
686 chromosome signal intensity in anaphase and the use of the full width at half maximum (FWHM)
687 as a measure of anaphase chromosome mass broadness. **(J)** Full width at half maximum of the
688 plotted intensities of separating chromosome masses of HeLa-Kyoto cells expressing KIF22-GFP
689 or KIF22-GFP T463A. Lines represent the mean and the shaded area denotes SEM. **(K)** Minimum
690 FWHM value, representing maximal anaphase chromosome compaction, between cells
691 expressing KIF22-GFP and KIF22-GFP T463A. p value from Mann-Whitney test. Bars represent
692 medians. Data in (J) and (K) represent 24-48 cells from 5 experiments per condition.

Figure 9

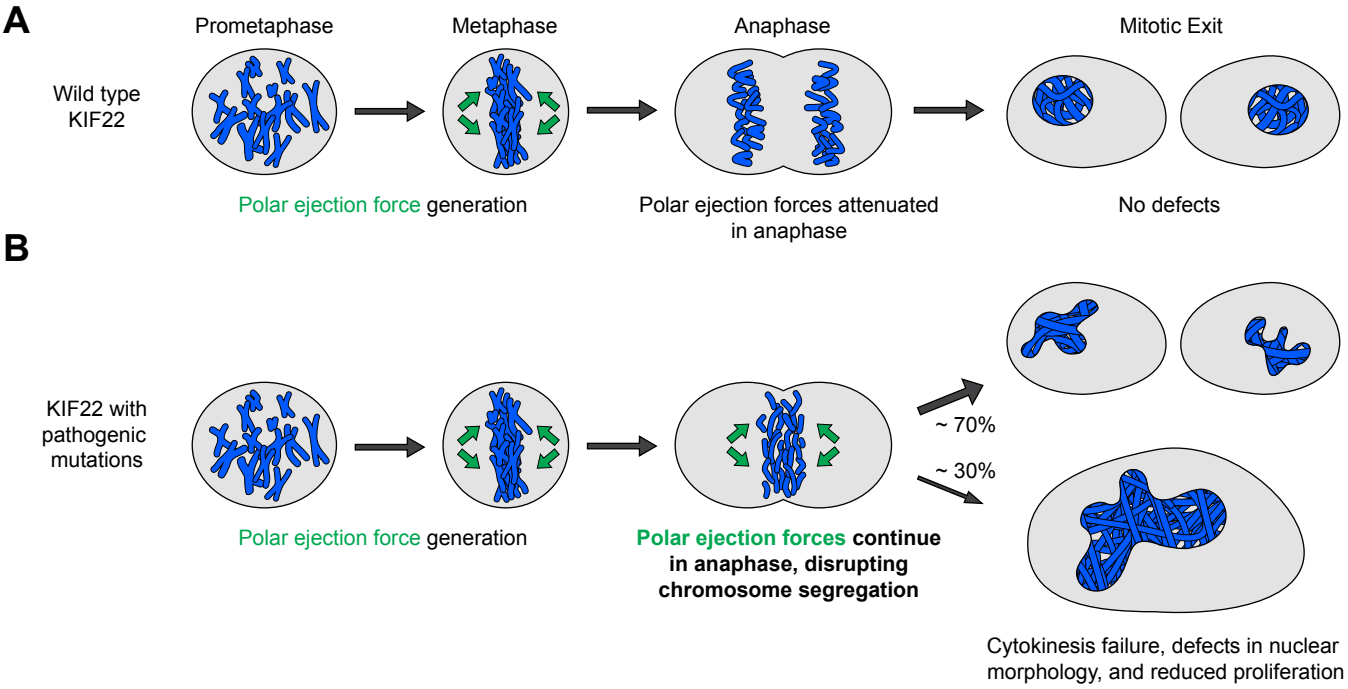
A
Prometaphase
Metaphase
Anaphase
Mitotic Exit
Wild type KIF22
Polar ejection force generation
Polar ejection forces attenuated in anaphase
No defects
B
KIF22 with pathogenic mutations
Polar ejection force generation
Polar ejection forces continue in anaphase, disrupting chromosome segregation
~ 70%
~ 30%
Cytokinesis failure, defects in nuclear morphology, and reduced proliferation

693 **Figure 9. Pathogenic mutations disrupt the anaphase, but not prometaphase, function of**
694 **KIF22.**
695 **(A)** Wild type KIF22 generates polar ejection forces to contribute to chromosome congression
696 and alignment in prometaphase. In anaphase, KIF22 inactivation results in the attenuation of polar
697 ejection forces (green arrows), allowing chromosomes to segregate toward the poles. Daughter
698 cells form regularly shaped nuclei and continue to proliferate. **(B)** In cells expressing KIF22 with
699 pathogenic (P148L, P148S, R149L, R149Q, V475G) or phosphomimetic (T463D) mutations,
700 prometaphase proceeds as in cells expressing wild type motor. Mutant KIF22 is capable of polar
701 ejection force generation. In anaphase, KIF22 fails to inactivate, resulting in continued generation
702 of polar ejection forces, which disrupts anaphase chromosome segregation. Daughter cells exhibit
703 nuclear morphology defects. In about 30% of cells, cytokinesis fails, and proliferation rates are
704 reduced.

705 **DISCUSSION**

706

707 We have determined that pathogenic mutations in KIF22 disrupt anaphase chromosome
708 segregation, causing chromosome recongression, nuclear morphology defects, reduced
709 proliferation, and, in a subset of cells, cytokinesis failure. Wild type KIF22 is inactivated in
710 anaphase (Soeda et al., 2016), resulting in an attenuation of polar ejection forces, which allows
711 chromosomes to move towards the spindle poles **(Figure 9A)**. The phenotypes we observe in
712 cells expressing KIF22-GFP with pathogenic mutations are consistent with KIF22 remaining
713 active in anaphase **(Figure 9B)**. Polar ejection forces could cause recongression by continuing
714 to push chromosomes away from the spindle poles during anaphase. These forces would result
715 in aberrant positioning of chromosomes during telophase and cytokinesis, which could cause the
716 nuclear morphology defects and cytokinesis failure we observe in cells expressing mutant KIF22-
717 GFP. Consistent with this model, mimicking phosphorylation of T463 to prevent KIF22 inactivation
718 in anaphase phenocopies the effects of pathogenic mutations. Thus, we conclude that pathogenic
719 mutations result in a gain of KIF22 function, consistent with findings that KIF22 mutations are
720 dominant in heterozygous patients (Boyden et al., 2011; Min et al., 2011; Tüysüz et al., 2014).

721 Mutations in both the motor domain (P148L, P148S, R149L, and R149Q) and the coiled-
722 coil domain (V475G) of KIF22 disrupt chromosome segregation in a manner consistent with a
723 failure of KIF22 inactivation in anaphase. This finding could contribute to our understanding of the
724 mechanism by which KIF22 is inactivated. Given that mutations in the tail and motor domain of
725 KIF22 both disrupt chromosome segregation, the tail and motor domain may interact to inactivate
726 the motor. Head-tail autoinhibition is a known regulatory mechanism of other members of the
727 kinesin superfamily (Blasius et al., 2021; Coy, Hancock, Wagenbach, & Howard, 1999; Espeut et
728 al., 2008; Friedman & Vale, 1999; Hammond, Blasius, Soppina, Cai, & Verhey, 2010; Hammond
729 et al., 2009; Imanishi, Endres, Gennerich, & Vale, 2006; Ren et al., 2018; Verhey & Hammond,
730 2009; Verhey et al., 1998), and disruption of autoinhibition can be a mechanism of disease
731 pathogenesis (Asselin et al., 2020; Bianchi et al., 2016; Blasius et al., 2021; Cheng et al., 2014;
732 van der Vaart et al., 2013). Mutations in either the tail or motor domain could disrupt this
733 interaction, preventing KIF22 inactivation in anaphase. As amino acids P148, R149, and V475
734 are highly conserved across species in members of the kinesin-10 family **(Figure 1C)**, this
735 inactivation mechanism may be present in these motors as well.

736 Alternatively, it has been proposed that the tail of KIF22 may interact with microtubules to
737 suspend polar ejection force generation (Soeda et al., 2016). In this framework, the mutation in
738 the tail of KIF22 (V745G) could disrupt anaphase chromosome segregation by altering this

739 interaction with microtubules. Motor domain mutations would not be expected to alter the
740 interaction of the tail with the surface of microtubules, and in this model would cause the same
741 cellular phenotype by altering KIF22 inactivation via a different mechanism, potentially related to
742 the mechanochemical cycle of the motor given the location of these mutations in the α2 helix.

743 While chromosomes in some cells, particularly those expressing KIF22-GFP at high
744 levels, completely failed to segregate and decondensed in the center of the spindle, most cells
745 demonstrated chromosome recongression wherein poleward motion of chromosomes begins, but
746 then chromosomes switch direction and move anti-poleward. These dynamics may be due to
747 differences in microtubule density closer to the poles compared to the center of the spindle. This
748 model is consistent with work demonstrating that in monopolar spindles, poleward movement of
749 chromosomes is limited by chromosomes reaching a threshold density of microtubules at which
750 polar ejection forces are sufficient to cause chromosomes to switch to anti-poleward movement
751 (Cassimeris, Rieder, & Salmon, 1994). We observed that chromosomes on the periphery of the
752 spindle remain closer to the poles while central chromosomes are pushed further away from the
753 poles during recongression in cells expressing KIF22-GFP with pathogenic mutations. This could
754 also be explained by the central chromosomes encountering a higher density of microtubules,
755 and KIF22 bound to these chromosomes therefore generating higher levels of polar ejection
756 forces. In addition, this mechanism is consistent with observations that oscillations of peripheral
757 chromosomes are reduced compared to chromosomes at the center of the spindle (Cameron et
758 al., 2006; Cimini, Cameron, & Salmon, 2004; Civelekoglu-Scholey et al., 2013; Stumpff, Dassow,
759 Wagenbach, Asbury, & Wordeman, 2008), which could also be explained by reduced peripheral
760 microtubule density limiting peripheral polar ejection force generation.

761 Our observation that the expression of KIF22-GFP with pathogenic mutations changes not
762 only the movements of chromosome arms and centromeres in anaphase, but also the movements
763 of the spindle poles, offers insight into the relative magnitude of polar ejection forces compared
764 to the forces generated by the sliding of antiparallel spindle microtubules to separate the spindle
765 poles in anaphase (Brust-Mascher, Civelekoglu-Scholey, Kwon, Mogilner, & Scholey, 2004; Fu
766 et al., 2009; Nislow, Lombillo, Kuriyama, & McIntosh, 1992; Sawin, LeGuellec, Philippe, &
767 Mitchison, 1992; Straight, Sedat, & Murray, 1998; Tanenbaum et al., 2009; van Heesbeen,
768 Tanenbaum, & Medema, 2014; Vukušić, Buđa, & Tolić, 2019; Vukušić, Ponjavić, Buđa, Risteski,
769 & Tolić, 2021). In cells expressing mutant KIF22-GFP, spindle pole separation stalled, and poles
770 moved closer to one another during anaphase chromosome recongression. This suggests that
771 the polar ejection forces collectively generated by mutant KIF22 motors are of greater magnitude
772 than the forces sliding the spindle poles apart during anaphase B. Although it is important to note

773 that this phenotype was observed with moderate overexpression of mutant KIF22, the observed
774 effects on spindle pole separation underscore the importance of KIF22 inactivation, and imply that
775 reducing polar ejection forces is required for both anaphase A and anaphase B.
776 Patients with mutations in KIF22 exhibit defects in skeletal development. The pathology
777 observed in the patient heterozygous for the V475G mutation differs from those seen in SEMDJL2
778 patients with motor domain mutations **(Figure 1E, 1F)** (Boyden et al., 2011; Min et al., 2011;
779 Tüysüz et al., 2014). However, a meaningful comparison of pathologies between patients is
780 limited both by the fact that only a single patient with a mutation in the tail of KIF22 has been
781 identified, and by the considerable variation in clinical presentation between patients with motor
782 domain mutations, even between patients with the same point mutation (Boyden et al., 2011; Min
783 et al., 2011; Tüysüz et al., 2014). The defects in chromosome segregation we observed in cells
784 expressing mutant KIF22-GFP may contribute to skeletal developmental pathogenesis. Mutations
785 could cause reduced proliferation of growth plate chondrocytes, which in turn could limit bone
786 growth. Disrupting cytokinesis in the growth plate causes shorter bones and stature in mice (Gan
787 et al., 2019), and mutations in KIF22 could affect development via this mechanism. The presence
788 of pathologies in other cartilaginous tissues, including the larynx and trachea, in patients with
789 mutations in the motor domain of KIF22 (Boyden et al., 2011) is also consistent with a disease
790 etiology based in aberrant chondrocyte proliferation. Defects in mitosis could result in tissue-
791 specific patient pathology based on differences in force balance within anaphase spindles in
792 different cell types arising from different expression or activity levels of mitotic force generators or
793 regulators. Growth plate chondrocytes, particularly, are organized into columns and must divide
794 under geometric constraints (Dodds, 1930), which could increase sensitivity to anaphase force
795 imbalances. Additionally, we cannot exclude the possibility that these mutations may affect the
796 function of interphase cells, which could affect development via a mechanism independent from
797 the effects of the mutations on mitosis. Future work will be required to distinguish among these
798 possible explanations.
799
800 **MATERIALS AND METHODS**
801 **Patient assessment**
802 Clinical exome sequencing was performed by the Department of Laboratory Medicine and
803 Pathology at Mayo Clinic in Rochester, Minnesota, USA as previously described (Cousin et al.,
804 2019). Carbohydrate deficient transferrin testing for congenital disorders of glycosylation was
805 performed at Mayo Clinic Laboratories, Rochester, Minnesota, USA (Lefeber, Morava, & Jaeken,
806 2011).

807

808 **Cell culture**

809 HeLa-Kyoto and RPE-1 cell lines were grown in Minimum Essential Media α (Gibco
810 #12561-056) supplemented with 10% fetal bovine serum (Gibco #16000-044) at 37°C with 5%
811 CO_2. Cell lines were validated by short tandem repeat (STR) DNA typing using the Promega
812 GenePrint 10 System according to the manufacturer's instructions (Promega #B9510). Cells were
813 cryopreserved in Recovery Cell Culture Freezing Medium (Gibco #12648-010). HeLa-Kyoto and
814 RPE-1 acceptor cell lines for recombination (both gifts from Ryoma Ohi, University of Michigan)
815 were maintained in media supplemented with 10 μg/mL blasticidin (Thermo Fisher Scientific
816 #R21001).

817

818 **Transfection**

819 siRNA transfection was performed using Lipofectamine RNAiMax Transfection Reagent
820 (Thermo Fisher Scientific #13778150) in Opti-MEM Reduced Serum Media (Gibco #31985-062).
821 KIF22 was targeted for siRNA-mediated depletion using a Silencer Validated siRNA (Ambion
822 #AM51331, sense sequence GCUGCUCUCUAGAGAUUGCTT). Control cells were transfected
823 with Silencer Negative Control siRNA #2 (Ambion #AM4613). DNA transfections were performed
824 using Lipofectamine LTX (Thermo Fisher Scientific #15338100) in Opti-MEM Reduced Serum
825 Media (Gibco #31985-062).

826

827 **Plasmids**

828 Plasmids related to the generation of inducible cell lines are described in Table 1. A C-
829 terminally tagged KIF22-GFP plasmid was constructed by adding EcoRI and KpnI sites to the
830 KIF22 open reading frame (from pJS2161 (Stumpff et al., 2012)), performing a restriction digest,
831 and ligating the products into a digested pEGFP-N2 vector (Clontech) (pAT4206). Site-directed
832 mutagenesis was performed to add silent mutations for siRNA resistance (pAT4226). The open
833 reading frame from pAT4226 and the pEM791 vector (Khandelia, Yap, & Makeyev, 2011) were
834 amplified and combined using Gibson Assembly (New England BioLabs) to generate a plasmid
835 for recombination-mediated construction of inducible cell lines (pAT4250). Site-directed
836 mutagenesis was performed on pAT4250 to generate plasmids encoding KIF22-GFP P148L,
837 P148S, R149L, R149Q, V475G, T463D, and T463A for recombination. See Table 1 for primer
838 sequences.

839 The mCh-CAAX plasmid was a gift from Alan Howe (University of Vermont). The mCh-
840 NLS plasmid was generated by Michael Davidson and obtained from Addgene (mCh-Nucleus-7,

841 #55110). The pericentrin-RFP plasmid (Gillingham & Munro, 2000) was a gift from Sean Munro
842 (MRC Laboratory of Molecular Biology). The CENPB-mCh plasmid (D. Liu et al., 2010) was
843 generated by Michael Lampson and obtained from Addgene (#45219).
844
845 **Generation of inducible cell lines**
846 Inducible cell lines were generated using recombination-mediated cassette exchange as
847 previously described (Khandelia et al., 2011). Briefly, plasmids (see Table 1) encoding siRNA-
848 resistant KIF22-GFP constructs were cotransfected with a plasmid encoding nuclear localized
849 Cre recombinase (pEM784) into HeLa-Kyoto (Sturgill, Norris, Guo, & Ohi, 2016) or RPE-1
850 acceptor cells using Lipofectamine LTX transfection (Thermo Fisher Scientific #15338100). For
851 HeLa-Kyoto cell lines, 24 hours after transfection cells were treated with 1 μg/mL puromycin
852 (Thermo Fisher Scientific #A11139-03) for 48 hours, then 2 μg/mL puromycin for 48 hours for
853 more stringent selection, and finally 1 μg/mL puromycin until puromycin-sensitive cells were
854 eliminated. Selection of RPE-1 cells was accomplished via treatment with 5 μg/mL puromycin for
855 48 hours beginning 24 hours after transfection, then 10 μg/mL puromycin for 48 hours, and finally
856 5 μg/mL puromycin until puromycin-sensitive cells were eliminated. Inducible cell lines were
857 maintained in puromycin (HeLa-Kyoto 1 μg/mL, RPE-1 5 μg/mL) for continued selection. To
858 confirm the sequence of inserted DNA in the selected cell populations, genomic DNA was
859 extracted using the QIAmp DNA Blood Mini Kit (Qiagen #51106) and subjected to sequencing
860 (Eurofins). Expression of inserted DNA sequences was induced via treatment with 2 μg/mL
861 doxycycline (Thermo Fisher Scientific #BP26531).
862
863 **Immunofluorescence**
864 For fixed cell imaging, cells were grown on 12 mm glass coverslips in 24-well plates. Cells
865 were fixed in 1% paraformaldehyde in ice-cold methanol for 10 minutes on ice. Cells were blocked
866 for 1 hour using 20% goat serum (Gibco #16210-064) in antibody dilution buffer (AbDil, 1% bovine
867 serum albumin (Sigma Aldrich #B4287), 0.1% Triton X-100 (Sigma Aldrich #93443), 0.02%
868 sodium azide (Fisher Scientific #BP9221) in TBS) and incubated with the following primary
869 antibodies for one hour at room temperature: mouse anti-α-tubulin (DM1α) 1:500 (Millipore Sigma
870 #T6199), rat anti-tubulin clone YL1/2 1:1500 (Millipore Sigma #MAB1864), rabbit anti-KIF22 1:500
871 (GeneTex #GTX112357), mouse anti-centrin 1:500 (Millipore Sigma #04-1624), or rabbit anti-
872 GFP 1:1000 (Invitrogen #A11121). Cells were incubated with secondary antibodies conjugated to
873 AlexaFluor 488, 594, or 647 (Invitrogen Molecular Probes #A11034, A11037, A21245, A11029,

874 A11032, A21236, A11007) for one hour at room temperature. Coverslips were mounted on slides
875 using Prolong Gold mounting medium with DAPI (Invitrogen Molecular Probes #P36935).
876
877 **Microscopy**
878 Images were acquired using a Nikon Ti-E or Ti-2E inverted microscope driven by NIS
879 Elements software (Nikon Instruments). Images were captured using a Clara cooled charge-
880 coupled device (CCD) camera (Andor) or Prime BSI scientific complementary metal-oxide-
881 semiconductor (sCMOS) camera (Teledyne Photometrics) with a Spectra-X light engine
882 (Lumencore). Samples were imaged using Nikon objectives Plan Apo 40X 0.95 numerical
883 aperture (NA), Plan Apo λ 60X 1.42 NA, and APO 100X 1.49 NA. For live imaging, cells were
884 imaged in CO_2-independent media (Gibco #18045-088) supplemented with 10% fetal bovine
885 serum (Gibco #16000-044) in a 37º C environmental chamber. Images were processed and
886 analyzed using Image J/FIJI (Schindelin et al., 2012; Schneider, Rasband, & Eliceiri, 2012).
887
888 **KIF22-GFP expression level quantitation**
889 HeLa-Kyoto or RPE-1 cells were treated with 2 μg/mL doxycycline to induce expression
890 and transfected with control or KIF22 siRNA approximately 24 hours prior to fixation. Metaphase
891 cells were imaged for measurement of KIF22 expression levels. Measurements of KIF22
892 immunofluorescence intensity were made in a background region of interest (ROI) containing no
893 cells and an ROI representing the chromosomes, identified by thresholding DAPI signal. The
894 mean background subtracted KIF22 signal on the chromosomes was calculated by subtracting
895 the product of the mean background intensity and the chromosome ROI area from the
896 chromosome ROI integrated density and dividing by the area of the chromosome ROI. KIF22
897 intensities were normalized to the mean KIF22 intensity in control cells (control knockdown,
898 uninduced) in each experimental replicate.
899
900 **Metaphase chromosome spreads**
901 RPE-1 cells were grown in 60 mm dishes for approximately 24 hours. Media was
902 exchanged to fresh growth media for 2 hours to promote mitosis. Cells were arrested in 0.02
903 μg/mL colcemid (Gibco KaryoMAX #15212012) for three hours at 37°C, then trypsinized, pelleted,
904 and gently re-suspended in 500 μL media. 5 mL 0.56% KCl hypotonic solution was added
905 dropwise to the cell suspension, which was then incubated for 15 minutes in a 37°C water bath.
906 Cells were pelleted, gently resuspended, and fixed via the addition of 1 mL ice-cold 3:1
907 methanol:glacial acetic acid. Cells were pelleted and resuspended in fixative an additional three

908 times, then stored at -20°C. Metaphase chromosome spreads were prepared by humidifying the
909 surface of glass slides by exposing them to the steam above a 50°C water bath, placing the slides
910 at an angle relative to the work surface, and dropping approximately 100 μL of ice-cold cell
911 suspension onto the slide from a height of approximately one foot. Slides were dried on a hot
912 plate, then covered with Prolong Gold mounting medium with DAPI (Invitrogen Molecular Probes
913 #P36935) and sealed.
914
915 **Fluorescence recovery after photobleaching**
916 HeLa-Kyoto cells were seeded in glass-bottom 35 mm dishes (Greiner Bio-One #627975
917 and #627965) and treated with 2 μg/mL doxycycline to induce expression 18-24 hours before
918 imaging. Cells were imaged at 5 second intervals for 25 seconds before bleaching, photobleached
919 using a point-focused 405 nm laser, and imaged at 20 second intervals for 10 minutes after
920 bleaching. Fluorescence intensities in bleached, unbleached, and background regions of each
921 frame were measured using a circular ROI, area 0.865 μm^2. For interphase and metaphase cells,
922 unbleached measurements were made on the opposite side of the nucleus or chromosome mass
923 as the bleached measurements. For anaphase cells, one segregating chromosome mass was
924 bleached, and unbleached measurements were made on the opposite chromosome mass.
925 Background intensities, measured in cell-free area, were subtracted from bleached and
926 unbleached intensities. Background-subtracted intensities were normalized to the intensity of the
927 first frame imaged.
928
929 **Polar ejection force assay**
930 HeLa-Kyoto cells were treated with 2 μg/mL doxycycline to induce expression and
931 transfected with control or KIF22 siRNA approximately 24 hours prior to fixation. Cells were
932 arrested in 100 μM monastrol (Selleckchem #S8439) for 2-3 hours before fixation. Monopolar
933 mitotic cells oriented perpendicular to the coverslip were imaged at the focal plane of the spindle
934 pole for polar ejection force measurements. A circular ROI with a 12.5 μm radius was centered
935 around the spindle pole of each cell, and the radial profile of DAPI signal intensity at distances
936 from the pole was measured (Radial Profile Plot plugin, https://imagej.nih.gov/ij/plugins/radial-
937 profile.html). The distance from the pole to the maximum DAPI signal was calculated for each cell
938 as a measure of relative polar ejection forces.
939
940 **Analyses of anaphase chromosome segregation**

941 HeLa-Kyoto or RPE-1 cells were treated with 2 μg/mL doxycycline to induce expression
942 approximately 18 hours before imaging. For HeLa-Kyoto cells, media was exchanged to CO_2-
943 indpendent media containing 2 μg/mL doxycycline and 100 nM SiR-Tubulin (Spirochrome
944 #SC002) approximately 1-1.5 hours before imaging. For RPE-1 cells, media was exchanged to
945 CO_2-indpendent media containing 2 μg/mL doxycycline, 20-100 nM SiR-Tubulin (Spirochrome
946 #SC002), and 10 μM verapamil (Spirochrome #SCV01) approximately 1.5-3 hours before
947 imaging. Cells were imaged at 1 minute time intervals. Distances between segregating
948 chromosome masses were measured by plotting the KIF22-GFP signal intensity along a line
949 drawn through both spindle poles (macro available at https://github.com/StumpffLab/Image-
950 Analysis). This data set was split at the center distance to generate two plots, each representing
951 one half-spindle/segregating chromosome mass. The distance between the maximum of each
952 intensity plot was calculated using MATLAB (Mathworks, Version R2018a) (script available at
953 https://github.com/StumpffLab/Image-Analysis). To assess the broadness of segregating
954 chromosome masses in cells expressing KIF22-GFP T463A, a Gaussian curve was fit to the same
955 intensity plots and the full width at half maximum was calculated in MATLAB.
956 To measure the movements of spindle poles and kinetochores in anaphase, HeLa-Kyoto
957 cells were seeded in glass-bottom 24-well plates (Cellvis #P24-1.5H-N) and cotransfected with
958 PCM-RFP and mCh-CENPB using Lipofectamine LTX (Thermo Fisher Scientific #15338100)
959 approximately 24 hours before imaging. Cells were treated with 2 μg/mL doxycycline to induce
960 expression approximately 12-18 hours before imaging. Cells were imaged at 20 second time
961 intervals. To more clearly visualize spindle poles and kinetochores, images of PCM-RFP and
962 mCh-CENPB signal were background subtracted by duplicating each frame, applying a gaussian
963 blur (sigma 30 pixels), and subtracting this blurred image from the original. For each frame, a line
964 was drawn between spindle poles (PCM-RFP signal) to measure the distance between them, and
965 the intensity of KIF22-GFP and mCh-CENPB along this line was plotted. These data sets were
966 split at the center distance to generate two plots, and the distance between plot maxima and the
967 distance from maxima to the spindle poles were calculated using MATLAB (scripts available at
968 https://github.com/StumpffLab/Image-Analysis).
969
970 **Assessment of cytokinesis failure**
971 To visualize cell boundaries, HeLa-Kyoto cells were transfected with mCh-CAAX using
972 Lipofectamine LTX approximately 24-32 hours before imaging and treated with 2 μg/mL
973 doxycycline approximately 8 hours before imaging. Cells were imaged at 3-minute intervals. Cells

974 were scored as failing cytokinesis if the product of mitosis was a single cell with a single boundary
975 of mCh-CAAX signal.
976
977 **Nuclear morphology quantification**
978 HeLa-Kyoto or RPE-1 cells were treated with 2 μg/mL doxycycline to induce expression
979 approximately 24 hours before fixation. Nuclear solidity was measured for each interphase
980 nucleus in each imaged field. The 5th percentile of solidity for control cells (transfected with control
981 siRNA and expressing GFP) was used as a threshold below which nuclear solidity was considered
982 abnormal.
983 To assess the ability of nuclei to retain nuclear-localized proteins, cells were transfected
984 with mCh-NLS using Lipofectamine LTX approximately 24-32 hours before imaging and treated
985 with 2 μg/mL doxycycline approximately 8 hours before imaging. Cells were imaged at 3-minute
986 intervals during and after division, and the presence of mCh-NLS signal in all nuclear structures
987 (KIF22-GFP positive regions) was assessed.
988
989 **Assessment of spindle dependence of nuclear morphology defects**
990 To assess whether nuclear morphology defects caused by KIF22 depend on force
991 generation within the mitotic spindle, cells were treated with 2 μg/mL doxycycline approximately
992 8 hours before imaging, SPY595-DNA (1X per manufacturer's instructions) (Spirochrome
993 #SC301) approximately 1.5-2 hours before imaging, and 500 nM nocodazole (Selleckchem
994 #S2775) and 900 nM reversine (Cayman Chemical #10004412) approximately 0.5-1 hour before
995 imaging. Cells were imaged at 5-minute intervals. Nuclear solidity was measured 15 minutes
996 before chromosome condensation and 100 minutes after chromosome decondensation.
997
998 **Proliferation assay**
999 HeLa-Kyoto cells were seeded in a 96-well plate and treated with 2 μg/mL doxycycline to
1000 induce expression or transfected with KIF22 siRNA approximately eight hours before the first
1001 assay timepoint. Automated bright field imaging using a Cytation 5 Cell Imaging Multi-Mode
1002 Reader (Biotek) (4X Plan Fluorite 0.13 NA objective (Olympus)) driven by Gen5 software (Biotek)
1003 was used to measure cell proliferation (Marquis et al., 2021). Images were collected every 4 hours
1004 for 96 hours. Gen5 software was used to process images and count the number of cells in each
1005 imaged field. Cell counts were normalized to the cell count in the first image acquired at time 0.
1006 Fold change at 96 hours was calculated by dividing the cell count at 96 hours by the cell count at
1007 time 0. Predicted cell counts at 48 hours were calculated using an experimentally determined

1008 doubling time of 20.72 hours for the control case where all cells divide ($Cells_T = 2^{(\frac{T}{20.72})}$), the case
1009 where nuclear morphology defects limit proliferation and 60% of cells do not divide ($Cells_T =$
1010 $1.4^{(\frac{T}{20.72})}$), and the case where cytokinesis failure limits proliferation and 30% of cells do not divide
1011 ($Cells_T = 1.7^{(\frac{T}{20.72})}$).
1012
1013 **Statistical analyses**
1014 Statistical tests were performed using GraphPad Prism software (GraphPad Software,
1015 Inc.), version 9.2.0. Specific statistical tests and n values for reported data are indicated in the
1016 figure legends. All data represent a minimum of three independent experiments.

Table 1

Plasmid	Description	Primers (5' to 3', Fw: Forward, Rev: Reverse)	Source
pEM784	nlCre recombinase	NA	Khandelia 2011 PMID 21768390
pEM791	EGFP for recombination	NA	Khandelia 2011 PMID 21768390
pJS2161	GFP-KIF22	NA	Stumpff 2012 PMID 22595673
pAT4206	KIF22-GFP	Fw: TACGTGGAATTCCACCATGGCCGCGGGCGGCTCGA Rev: GTGACTGGTACCTGGAGGCGCCACAGCGCTGGC	This study
pAT4226	KIF22-GFP, siRNA resistant	Fw: GGGCATGGACAGCTGCTCACTCGAAATCGCTAACTGGAGGA ACCAC Rev: GTGGTTCCTCCAGTTAGCGATTTCGAGTGAGCAGCTGTCCA TGCCC	This study
pAT4250	KIF22-GFP, siRNA resistant, for recombination	Fragment Fw: CTGGGCACCACCATGGCCGCG Fragment Rev: GCTAGCTCGATTACTTGTACAGCTCGTCCATGCC Vector Fw: GTACAAGTAATCGAGCTAGCATATGGATCCATATAACT Vector Rev: CATGGTGGTGCCCAGTGCCTCACGACC	This study
pAT4251	KIF22-GFP R149Q, siRNA resistant, for recombination	Fw: GGGGTGATCCCGCAGGCTCTCATGGAC Rev: GTCCATGAGAGCCTGCGGGATCACCCC	This study
pAT4258	KIF22-GFP V475G, siRNA resistant, for recombination	Fw: TGCTAATGAAGACAGGAGAAGAGAAGGACCT Rev: AGGTCCTTCTCTTCTCCTGTCTTCATTAGCA	This study
pAT4260	KIF22-GFP T463D, siRNA resistant, for recombination	Fw: CCCCTCTGTTGAGTGACCCAAAGCGAGAGC Rev: GCTCTCGCTTTGGGTCACTCAACAGAGGGG	This study
pAT4261	KIF22-GFP T463A, siRNA resistant, for recombination	Fw: CCTCTGTTGAGTGCCCCAAAGCGAG Rev: CTCGCTTTGGGGCACTCAACAGAGG	This study
pAT4264	KIF22-GFP R149L, siRNA resistant, for recombination	Fw: GGGTGATCCCGCTGGCTCTCATGGAC Rev: GTCCATGAGAGCCAGCGGGATCACCC	This study
pAT4269	KIF22-GFP P148L, siRNA resistant, for recombination	Fw: CCTGGGGTGATCCTGCGGGCTCTCATG Rev: CATGAGAGCCCGCAGGATCACCCCAGG	This study
pAT4270	KIF22-GFP P148S, siRNA resistant, for recombination	Fw: CTGGGGTGATCTCGCGGGCTCTCATG Rev: CATGAGAGCCCGCGAGATCACCCCAG	This study

1017 **ACKNOWLEDGEMENTS**

1018 This work was supported by NIH F31AR074887 to AFT and NIH R01GM121491 to JKS.
1019 We thank the Mayo Clinic Center for Individualized Medicine (CIM) for supporting this research
1020 through the CIM Investigative and Functional Genomics program. We thank Alan Howe for the
1021 mCh-CAAX plasmid, and Ryoma Ohi for reagents and acceptor cells for recombination-mediated
1022 cassette exchange. We thank Rachel Stadler for technical assistance with data analysis and
1023 thank Laura Reinholdt and Matthew Warman for constructive discussions regarding this work.

1024

1025 **COMPETING INTERESTS**

1026 The authors declare no competing interests.

1027

1028 **VIDEO LEGENDS**

1029 **Video 1. Fluorescence recovery after photobleaching of KIF22-GFP.**
1030 Fluorescence recovery after photobleaching (FRAP) in HeLa-Kyoto cells expressing KIF22-GFP
1031 (top), KIF22-GFP R149Q (middle), or KIF22-GFP V475G (bottom). Cells represent interphase
1032 (left), metaphase (middle), or anaphase (right). Bleaching occurred at time zero. Scale bar 10 μm.
1033 Cells were imaged at 5 second intervals for 25 seconds before bleaching, photobleached, and
1034 imaged at 20 second intervals for 10 minutes after bleaching. Playback at 10 frames per second.

1035

1036 **Video 2. Anaphase in HeLa-Kyoto cells.**
1037 Anaphase chromosome segregation in HeLa-Kyoto cells expressing KIF22-GFP (left), KIF22-
1038 GFP R149Q (middle), or KIF22-GFP V475G (right). Magenta: SiR-Tubulin, green: KIF22-GFP.
1039 Times indicate minutes after anaphase onset. Scale bar 5 μm. Cells were imaged at 1 minute
1040 intervals. Playback at 10 frames per second (600X real time).

1041

1042 **Video 3. Anaphase in RPE-1 cells.**
1043 Anaphase chromosome segregation in RPE-1 cells expressing KIF22-GFP (left), KIF22-GFP
1044 R149Q (middle), or KIF22-GFP V475G (right). Magenta: SiR-Tubulin, green: KIF22-GFP. Times
1045 indicate minutes after anaphase onset. Scale bar 5 μm. Cells were imaged at 1 minute intervals.
1046 Playback at 10 frames per second (600X real time).

1047

1048 **Video 4. Anaphase spindle pole separation.**

1049 Anaphase in HeLa-Kyoto cells expressing pericentrin-RFP (magenta), CENPB-mCh (magenta),
1050 and KIF22-GFP (cyan). Times indicate seconds after anaphase onset. Scale bar 5 μm. Cells were
1051 imaged at 20 second intervals. Playback at 15 frames per second (300X real time).
1052
1053 **Video 5. Cytokinesis and cytokinesis failure.**
1054 Mitosis and cytokinesis in HeLa-Kyoto cells expressing KIF22-GFP (left), KIF22-GFP R149Q
1055 (middle), or KIF22-GFP V475G (right) (all KIF22-GFP represented in green) and mCh-CAAX
1056 (magenta). Scale bar 10 μm. Cells were imaged at 3 minute intervals. Playback at 25 frames per
1057 second (4500X real time).
1058
1059 **REFERENCES**
1060

1061 Adzhubei, I. A., Schmidt, S., Peshkin, L., Ramensky, V. E., Gerasimova, A., Bork, P., et al.
1062 (2010). A method and server for predicting damaging missense mutations. *Nature Methods*,
1063 *7*(4), 248–249. http://doi.org/10.1038/nmeth0410-248
1064 Antonio, C., Ferby, I., Wilhelm, H., Jones, M., Karsenti, E., Nebreda, A. R., & Vernos, I. (2000).
1065 Xkid, a chromokinesin required for chromosome alignment on the metaphase plate. *Cell*,
1066 *102*(4), 425–435. http://doi.org/10.1016/s0092-8674(00)00048-9
1067 Asselin, L., Alvarez, J. R., Heide, S., Bonnet, C. S., Tilly, P., Vitet, H., et al. (2020). Mutations in
1068 the KIF21B kinesin gene cause neurodevelopmental disorders through imbalanced
1069 canonical motor activity. *Nature Communications*, 1–18. http://doi.org/10.1038/s41467-020-
1070 16294-6
1071 Bianchi, S., van Riel, W. E., Kraatz, S. H. W., Olieric, N., Frey, D., Katrukha, E. A., et al. (2016).
1072 Structural basis for misregulation of kinesin KIF21A autoinhibition by CFEOM1 disease
1073 mutations. *Scientific Reports*, *6*(1), 30668–16. http://doi.org/10.1038/srep30668
1074 Bieling, P., Kronja, I., & Surrey, T. (2010). Microtubule Motility on Reconstituted Meiotic
1075 Chromatin. *Current Biology*, *20*(8), 763–769. http://doi.org/10.1016/j.cub.2010.02.067
1076 Blasius, T. L., Yue, Y., Prasad, R., Liu, X., Gennerich, A., & Verhey, K. J. (2021). Sequences in
1077 the stalk domain regulate auto-inhibition and ciliary tip localization of the immotile kinesin-4
1078 KIF7. *Journal of Cell Science*, *134*(13). http://doi.org/10.1242/jcs.258464
1079 Bodnar, A. G., Ouellette, M., Frolkis, M., Holt, S. E., Chiu, C. P., Morin, G. B., et al. (1998).
1080 Extension of life-span by introduction of telomerase into normal human cells. *Science (New*
1081 *York, N.Y.)*, *279*(5349), 349–352. http://doi.org/10.1126/science.279.5349.349
1082 Boyden, E. D., Campos-Xavier, A. B., Kalamajski, S., Cameron, T. L., Suarez, P., Tanackovic,
1083 G., et al. (2011). Recurrent dominant mutations affecting two adjacent residues in the motor
1084 domain of the monomeric kinesin KIF22 result in skeletal dysplasia and joint laxity.
1085 *American Journal of Human Genetics*, *89*(6), 767–772.
1086 http://doi.org/10.1016/j.ajhg.2011.10.016
1087 Brouhard, G. J., & Hunt, A. J. (2005). Microtubule movements on the arms of mitotic
1088 chromosomes: polar ejection forces quantified in vitro. *Proceedings of the National*
1089 *Academy of Sciences*, *102*(39), 13903–13908. http://doi.org/10.1073/pnas.0506017102
1090 Brust-Mascher, I., Civelekoglu-Scholey, G., Kwon, M., Mogilner, A., & Scholey, J. M. (2004).
1091 Model for anaphase B: role of three mitotic motors in a switch from poleward flux to spindle
1092 elongation. *Proceedings of the National Academy of Sciences*, *101*(45), 15938–15943.
1093 http://doi.org/10.1073/pnas.0407044101

Cameron, L. A., Yang, G., Cimini, D., Canman, J. C., Kisurina-Evgenieva, O., Khodjakov, A., et al. (2006). Kinesin 5-independent poleward flux of kinetochore microtubules in PtK1 cells. *The Journal of Cell Biology*, *173*(2), 173–179. http://doi.org/10.1083/jcb.200601075

Cassimeris, L., Rieder, C. L., & Salmon, E. D. (1994). Microtubule Assembly and Kinetochore Directional Instability in Vertebrate Monopolar Spindles - Implications for the Mechanism of Chromosome Congression. *Journal of Cell Science*, *107*, 285–297.

Cheng, L., Desai, J., Miranda, C. J., Duncan, J. S., Qiu, W., Nugent, A. A., et al. (2014). Human CFEOM1 Mutations Attenuate KIF21A Autoinhibition and Cause Oculomotor Axon Stalling. *Neuron*, *82*(2), 334–349. http://doi.org/10.1016/j.neuron.2014.02.038

Cimini, D., Cameron, L. A., & Salmon, E. D. (2004). Anaphase spindle mechanics prevent mis-segregation of merotelically oriented chromosomes. *Current Biology*, *14*(23), 2149–2155. http://doi.org/10.1016/j.cub.2004.11.029

Civelekoglu-Scholey, G., He, B., Shen, M., Wan, X., Roscioli, E., Bowden, B., & Cimini, D. (2013). Dynamic bonds and polar ejection force distribution explain kinetochore oscillations in PtK1 cells. *The Journal of Cell Biology*, *201*(4), 577–593. http://doi.org/10.1083/jcb.201301022

Cousin, M. A., Conboy, E., Wang, J.-S., Lenz, D., Schwab, T. L., Williams, M., et al. (2019). RINT1 bi-allelic variations cause infantile-onset recurrent acute liver failure and skeletal abnormalities. *American Journal of Human Genetics*, *105*(1), 108–121. http://doi.org/10.1016/j.ajhg.2019.05.011

Coy, D. L., Hancock, W. O., Wagenbach, M., & Howard, J. (1999). Kinesin's tail domain is an inhibitory regulator of the motor domain. *Nature Cell Biology*, *1*(5), 288–292. http://doi.org/10.1038/13001

Dodds, G. S. (1930). Row formation and other types of arrangement of cartilage cells in endochondral ossification. *The Anatomical Record*, *46*(4), 385–399. http://doi.org/10.1002/ar.1090460409

Espeut, J., Gaussen, A., Bieling, P., Morin, V., Prieto, S., Fesquet, D., et al. (2008). Phosphorylation relieves autoinhibition of the kinetochore motor Cenp-E. *Molecular Cell*, *29*(5), 637–643. http://doi.org/10.1016/j.molcel.2008.01.004

Friedman, D. S., & Vale, R. D. (1999). Single-molecule analysis of kinesin motility reveals regulation by the cargo-binding tail domain. *Nature Cell Biology*, *1*(5), 293–297. http://doi.org/10.1038/13008

Fu, C., Ward, J. J., Loiodice, I., Velve-Casquillas, G., Nedelec, F. J., & Tran, P. T. (2009). Phospho-Regulated Interaction between Kinesin-6 Klp9p and Microtubule Bundler Ase1p Promotes Spindle Elongation. *Developmental Cell*, *17*(2), 257–267. http://doi.org/10.1016/j.devcel.2009.06.012

Funabiki, H., & Murray, A. W. (2000). The Xenopus chromokinesin Xkid is essential for metaphase chromosome alignment and must be degraded to allow anaphase chromosome movement. *Cell*, *102*(4), 411–424.

Gan, H., Xue, W., Gao, Y., Zhu, G., Chan, D., Cheah, K. S. E., & Huang, J. (2019). KIF5B modulates central spindle organization in late-stage cytokinesis in chondrocytes. *Cell & Bioscience*, 1–16. http://doi.org/10.1186/s13578-019-0344-5

Germani, A., Bruzzoni-Giovanelli, H., Fellous, A., Gisselbrecht, S., Varin-Blank, N., & Calvo, F. (2000). SIAH-1 interacts with alpha-tubulin and degrades the kinesin Kid by the proteasome pathway during mitosis. *Oncogene*, *19*(52), 5997–6006. http://doi.org/10.1038/sj.onc.1204002

Gillingham, A. K., & Munro, S. (2000). The PACT domain, a conserved centrosomal targeting motif in the coiled-coil proteins AKAP450 and pericentrin. *EMBO Reports*, *1*(6), 524–529. http://doi.org/10.1093/embo-reports/kvd105

Haila, S., Hästbacka, J., Böhling, T., Karjalainen-Lindsberg, M. L., Kere, J., & Saarialho-Kere, U. (2001). SLC26A2 (diastrophic dysplasia sulfate transporter) is expressed in developing and

mature cartilage but also in other tissues and cell types. *The Journal of Histochemistry and Cytochemistry : Official Journal of the Histochemistry Society*, *49*(8), 973–982. http://doi.org/10.1177/002215540104900805

Hammond, J. W., Blasius, T. L., Soppina, V., Cai, D., & Verhey, K. J. (2010). Autoinhibition of the kinesin-2 motor KIF17 via dual intramolecular mechanisms. *The Journal of Cell Biology*, *189*(6), 1013–1025. http://doi.org/10.1083/jcb.201001057

Hammond, J. W., Cai, D., Blasius, T. L., Li, Z., Jiang, Y., Jih, G. T., et al. (2009). Mammalian Kinesin-3 Motors Are Dimeric In Vivo and Move by Processive Motility upon Release of Autoinhibition. *PLOS Biology*, *7*(3), e1000072–14. http://doi.org/10.1371/journal.pbio.1000072

Hatch, E. M., Fischer, A. H., Deerinck, T. J., & Hetzer, M. W. (2013). Catastrophic nuclear envelope collapse in cancer cell micronuclei. *Cell*, *154*(1), 47–60. http://doi.org/10.1016/j.cell.2013.06.007

Hershko, A. (1999). Mechanisms and regulation of the degradation of cyclin B. *Philosophical Transactions of the Royal Society of London. Series B, Biological Sciences*, *354*(1389), 1571–5– discussion 1575–6. http://doi.org/10.1098/rstb.1999.0500

Iemura, K., & Tanaka, K. (2015). Chromokinesin Kid and kinetochore kinesin CENP-E differentially support chromosome congression without end-on attachment to microtubules. *Nature Communications*, *6*, 1–11. http://doi.org/10.1038/ncomms7447

Imanishi, M., Endres, N. F., Gennerich, A., & Vale, R. D. (2006). Autoinhibition regulates the motility of the C. elegans intraflagellar transport motor OSM-3. *The Journal of Cell Biology*, *174*(7), 931–937. http://doi.org/10.1083/jcb.200605179

Khandelia, P., Yap, K., & Makeyev, E. V. (2011). Streamlined platform for short hairpin RNA interference and transgenesis in cultured mammalian cells. *Proceedings of the National Academy of Sciences of the United States of America*, *108*(31), 12799–12804. http://doi.org/10.1073/pnas.1103532108

Lefeber, D. J., Morava, E., & Jaeken, J. (2011). How to find and diagnose a CDG due to defective N-glycosylation. *Journal of Inherited Metabolic Disease*, *34*(4), 849–852. http://doi.org/10.1007/s10545-011-9370-0

Levesque, A. A., & Compton, D. A. (2001). The chromokinesin Kid is necessary for chromosome arm orientation and oscillation, but not congression, on mitotic spindles. *The Journal of Cell Biology*, *154*(6), 1135–1146. http://doi.org/10.1083/jcb.200106093

Levesque, A. A., Howard, L., Gordon, M. B., & Compton, D. A. (2003). A functional relationship between NuMA and kid is involved in both spindle organization and chromosome alignment in vertebrate cells. *Molecular Biology of the Cell*, *14*(9), 3541–3552. http://doi.org/10.1091/mbc.E03-02-0082

Liu, D., Vleugel, M., Backer, C. B., Hori, T., Fukagawa, T., Cheeseman, I. M., & Lampson, M. A. (2010). Regulated targeting of protein phosphatase 1 to the outer kinetochore by KNL1 opposes Aurora B kinase. *The Journal of Cell Biology*, *188*(6), 809–820. http://doi.org/10.1083/jcb.201001006

Liu, Y., Mi, Y., Mueller, T., Kreibich, S., Williams, E. G., Van Drogen, A., et al. (2018). Genomic, proteomic and phenotypic heterogeneity in HeLa cells across laboratories: implications for reproducibility of research results. *bioRxiv*, 307421. http://doi.org/10.1101/307421

Marquis, C., Fonseca, C. L., Queen, K. A., Wood, L., Vandal, S. E., Malaby, H. L. H., et al. (2021). Chromosomally unstable tumor cells specifically require KIF18A for proliferation. *Nature Communications*, 1–14. http://doi.org/10.1038/s41467-021-21447-2

Marshall, W. F., Marko, J. F., Agard, D. A., & Sedat, J. W. (2001). Chromosome elasticity and mitotic polar ejection force measured in living Drosophila embryos by four-dimensional microscopy-based motion analysis. *Current Biology*, *11*(8), 569–578. http://doi.org/10.1016/s0960-9822(01)00180-4

Min, B.-J., Kim, N., Chung, T., Kim, O.-H., Nishimura, G., Chung, C. Y., et al. (2011). Whole-exome sequencing identifies mutations of KIF22 in spondyloepimetaphyseal dysplasia with joint laxity, leptodactylic type. *American Journal of Human Genetics*, *89*(6), 760–766. http://doi.org/10.1016/j.ajhg.2011.10.015

Morgan, D. O. (1995). Principles of CDK regulation. *Nature*, *374*(6518), 131–134. http://doi.org/10.1038/374131a0

Nislow, C., Lombillo, V. A., Kuriyama, R., & McIntosh, J. R. (1992). A plus-end-directed motor enzyme that moves antiparallel microtubules in vitro localizes to the interzone of mitotic spindles. *Nature*, *359*(6395), 543–547. http://doi.org/10.1038/359543a0

Ohsugi, M., Adachi, K., Horai, R., Kakuta, S., Sudo, K., Kotaki, H., et al. (2008). Kid-mediated chromosome compaction ensures proper nuclear envelope formation. *Cell*, *132*(5), 771–782. http://doi.org/10.1016/j.cell.2008.01.029

Ohsugi, M., Tokai-Nishizumi, N., Shiroguchi, K., Toyoshima, Y. Y., Inoue, J.-I., & Yamamoto, T. (2003). Cdc2-mediated phosphorylation of Kid controls its distribution to spindle and chromosomes. *The EMBO Journal*, *22*(9), 2091–2103. http://doi.org/10.1093/emboj/cdg208

Ren, J., Wang, S., Chen, H., Wang, W., Huo, L., & Feng, W. (2018). Coiled-coil 1-mediated fastening of the neck and motor domains for kinesin-3 autoinhibition. *Proceedings of the National Academy of Sciences of the United States of America*, *115*(51), E11933–E11942. http://doi.org/10.1073/pnas.1811209115

Rieder, C. L., & Salmon, E. D. (1994). Motile kinetochores and polar ejection forces dictate chromosome position on the vertebrate mitotic spindle. *The Journal of Cell Biology*, *124*(3), 223–233. http://doi.org/10.1083/jcb.124.3.223

Rieder, C. L., Davison, E. A., Jensen, L. C., Cassimeris, L., & Salmon, E. D. (1986). Oscillatory movements of monooriented chromosomes and their position relative to the spindle pole result from the ejection properties of the aster and half-spindle. *The Journal of Cell Biology*, *103*(2), 581–591. http://doi.org/10.1083/jcb.103.2.581

Ris, H. (1949). The anaphase movement of chromosomes in the spermatocytes of the grasshopper. *The Biological Bulletin*, *96*(1), 90–106.

Rossi, A., & Superti-Furga, A. (2001). Mutations in the diastrophic dysplasia sulfate transporter (DTDST) gene (SLC26A2): 22 novel mutations, mutation review, associated skeletal phenotypes, and diagnostic relevance. *Human Mutation*, *17*(3), 159–171. http://doi.org/10.1002/humu.1

Samwer, M., Schneider, M. W. G., Hoefler, R., Schmalhorst, P. S., Jude, J. G., Zuber, J., & Gerlich, D. W. (2017). DNA cross-bridging shapes a single nucleus from a set of mitotic chromosomes. *Cell*, *170*(5), 956–972.e23. http://doi.org/10.1016/j.cell.2017.07.038

Sawin, K. E., LeGuellec, K., Philippe, M., & Mitchison, T. J. (1992). Mitotic spindle organization by a plus-end-directed microtubule motor. *Nature*, *359*(6395), 540–543. http://doi.org/10.1038/359540a0

Schindelin, J., Arganda-Carreras, I., Frise, E., Kaynig, V., Longair, M., Pietzsch, T., et al. (2012). Fiji: an open-source platform for biological-image analysis. *Nature Methods*, *9*(7), 676–682. http://doi.org/10.1038/nmeth.2019

Schneider, C. A., Rasband, W. S., & Eliceiri, K. W. (2012). NIH Image to ImageJ: 25 years of image analysis. *Nature Methods*, 1–5. http://doi.org/10.1038/nmeth.2089

Schwarz, J. M., Rödelsperger, C., Schuelke, M., & Seelow, D. (2010). MutationTaster evaluates disease-causing potential of sequence alterations. *Nature Publishing Group*, 1–2. http://doi.org/10.1038/nmeth0810-575

Serra-Marques, A., Houtekamer, R., Hintzen, D., Canty, J. T., Yildiz, A., & Dumont, S. (2020). The mitotic protein NuMA plays a spindle-independent role in nuclear formation and mechanics. *The Journal of Cell Biology*, *219*(12), 348–23. http://doi.org/10.1083/jcb.202004202

Shiroguchi, K., Ohsugi, M., Edamatsu, M., Yamamoto, T., & Toyoshima, Y. Y. (2003). The second microtubule-binding site of monomeric Kid enhances the microtubule affinity. *The Journal of Biological Chemistry*, *278*(25), 22460–22465. http://doi.org/10.1074/jbc.M212274200

Soeda, S., Yamada-Nomoto, K., & Ohsugi, M. (2016). The microtubule-binding and coiled-coil domains of Kid are required to turn off the polar ejection force at anaphase. *Journal of Cell Science*, *129*(19), 3609–3619. http://doi.org/10.1242/jcs.189969

Straight, A. F., Sedat, J. W., & Murray, A. W. (1998). Time-lapse microscopy reveals unique roles for kinesins during anaphase in budding yeast. *The Journal of Cell Biology*, *143*(3), 687–694. http://doi.org/10.1083/jcb.143.3.687

Stumpff, J., Dassow, von, G., Wagenbach, M., Asbury, C., & Wordeman, L. (2008). The kinesin-8 Motor Kif18A suppresses kinetochore movements to control mitotic chromosome alignment. *Developmental Cell*, *14*(2), 252–262. http://doi.org/10.1016/j.devcel.2007.11.014

Stumpff, J., Wagenbach, M., Franck, A., Asbury, C. L., & Wordeman, L. (2012). Kif18A and chromokinesins confine centromere movements via microtubule growth suppression and spatial control of kinetochore tension. *Developmental Cell*, *22*(5), 1017–1029. http://doi.org/10.1016/j.devcel.2012.02.013

Sturgill, E. G., Norris, S. R., Guo, Y., & Ohi, R. (2016). Kinesin-5 inhibitor resistance is driven by kinesin-12. *The Journal of Cell Biology*, *213*(2), 213–227. http://doi.org/10.1083/jcb.201507036

Su, K.C., Barry, Z., Schweizer, N., Maiato, H., Bathe, M., & Cheeseman, I. M. (2016). A regulatory switch alters chromosome motions at the metaphase-to-anaphase transition. *Cell Reports*, *17*(7), 1728–1738. http://doi.org/10.1016/j.celrep.2016.10.046

Takagi, J., Itabashi, T., Suzuki, K., & Ishiwata, S. (2013). Chromosome position at the spindle equator is regulated by chromokinesin and a bipolar microtubule array. *Scientific Reports*, *3*, 746–7. http://doi.org/10.1038/srep02808

Tanenbaum, M. E., Macůrek, L., Janssen, A., Geers, E. F., Alvarez-Fernández, M., & Medema, R. H. (2009). Kif15 cooperates with Eg5 to promote bipolar spindle assembly. *Current Biology*, *19*(20), 1703–1711. http://doi.org/10.1016/j.cub.2009.08.027

Tokai, N., Fujimoto-Nishiyama, A., Toyoshima, Y., Yonemura, S., Tsukita, S., Inoue, J., & Yamamoto, T. (1996). Kid, a novel kinesin-like DNA binding protein, is localized to chromosomes and the mitotic spindle. *The EMBO Journal*, *15*(3), 457–467.

Tokai-Nishizumi, N., Ohsugi, M., Suzuki, E., & Yamamoto, T. (2005). The chromokinesin kid is required for maintenance of proper metaphase spindle size. *Molecular Biology of the Cell*, *16*(11), 5455–5463. http://doi.org/10.1091/mbc.E05-03-0244

Tüysüz, B., Yilmaz, S., Erener-Ercan, T., Bilguvar, K., & Günel, M. (2014). Spondyloepimetaphyseal dysplasia with joint laxity, leptodactylic type: longitudinal observation of radiographic findings in a child heterozygous for a KIF22 mutation. *Pediatric Radiology*, *45*(5), 771–776. http://doi.org/10.1007/s00247-014-3159-x

Uhlen, M., Fagerberg, L., Hallström, B. M., Lindskog, C., Oksvold, P., Mardinoglu, A., et al. (2015). Tissue-based map of the human proteome. *Science (New York, N.Y.)*, *347*(6220), 1260419–1260419. http://doi.org/10.1126/science.1260419

van der Vaart, B., van Riel, W. E., Doodhi, H., Kevenaar, J. T., Katrukha, E. A., Gumy, L., et al. (2013). CFEOM1-associated kinesin KIF21A is a cortical microtubule growth inhibitor. *Developmental Cell*, *27*(2), 145–160. http://doi.org/10.1016/j.devcel.2013.09.010

van Heesbeen, R. G. H. P., Tanenbaum, M. E., & Medema, R. H. (2014). Balanced activity of three mitotic motors is required for bipolar spindle assembly and chromosome segregation. *Cell Reports*, *8*(4), 948–956. http://doi.org/10.1016/j.celrep.2014.07.015

Vaser, R., Adusumalli, S., Leng, S. N., Sikic, M., & Ng, P. C. (2015). SIFT missense predictions for genomes. *Nature Protocols*, *11*(1), 1–9. http://doi.org/10.1038/nprot.2015-123

Verhey, K. J., & Hammond, J. W. (2009). Cytoskeletal motors: Traffic control: regulation of kinesin motors, 1–13. http://doi.org/10.1038/nrm2782

Verhey, K. J., Lizotte, D. L., Abramson, T., Barenboim, L., Schnapp, B. J., & Rapoport, T. A. (1998). Light chain-dependent regulation of Kinesin's interaction with microtubules. *The Journal of Cell Biology*, *143*(4), 1053–1066. http://doi.org/10.1083/jcb.143.4.1053

Vukušić, K., Buđa, R., & Tolić, I. M. (2019). Force-generating mechanisms of anaphase in human cells. *Journal of Cell Science*, *132*(18), jcs231985–11. http://doi.org/10.1242/jcs.231985

Vukušić, K., Ponjavić, I., Buđa, R., Risteski, P., & Tolić, I. M. (2021). Microtubule-sliding modules based on kinesins EG5 and PRC1-dependent KIF4A drive human spindle elongation. *Developmental Cell*, 1–42. http://doi.org/10.1016/j.devcel.2021.04.005

Wandke, C., Barisic, M., Sigl, R., Rauch, V., Wolf, F., Amaro, A. C., et al. (2012). Human chromokinesins promote chromosome congression and spindle microtubule dynamics during mitosis. *The Journal of Cell Biology*, *198*(5), 847–863. http://doi.org/10.1083/jcb.201110060

Yajima, J., Edamatsu, M., Watai-Nishii, J., Tokai-Nishizumi, N., Yamamoto, T., & Toyoshima, Y. Y. (2003). The human chromokinesin Kid is a plus end-directed microtubule-based motor. *The EMBO Journal*, *22*(5), 1067–1074. http://doi.org/10.1093/emboj/cdg102

Yount, A. L., Zong, H., & Walczak, C. E. (2015). Regulatory mechanisms that control mitotic kinesins. *Experimental Cell Research*, *334*(1), 70–77. http://doi.org/10.1016/j.yexcr.2014.12.015

Zhang, P., Knowles, B. A., Goldstein, L. S., & Hawley, R. S. (1990). A kinesin-like protein required for distributive chromosome segregation in Drosophila. *Cell*, *62*(6), 1053–1062.